Check for updates

Thermoelectrics Hot Paper

How to cite: *Angew. Chem. Int. Ed.* **2022,** *61,* e202212885
International Edition: doi.org/10.1002/anie.202212885
German Edition: doi.org/10.1002/ange.202212885

Realizing $zT > 2$ in Environment-Friendly Monoclinic Cu_2S—Tetragonal $Cu_{1.96}S$ Nano-Phase Junctions for Thermoelectrics

Xiaokun Li[+], Yue Lou[+], Kangpeng Jin, Liangwei Fu, Pengfei Xu, Zhan Shi, Tianli Feng, and Biao Xu**

Abstract: Phase-junction nanocomposites, made of nanograins with the same composition but different phases, offer a platform to optimize the physiochemical performance of materials. Herein, we demonstrate a straightforward strategy to synthesize $Cu_{2-x}S$ phase-junction nanocomposites by retaining surface 1-dodecanethiol (DDT) ligands, in contrast to the traditional method that strips the ligands. As a result, phase junctions between a conventional monoclinic (m) phase and an unconventional metastable tetragonal (t) phase are obtained. The significantly improved power factor is obtained due to the doping of the t-phase. The phase-junction interfaces reduce thermal conductivity. Finally, surface regulation of phase junctions pushes the peak zT to 2.1 at 932 K, being the highest reported for environment-friendly metal sulfides. This work provides a paradigm to optimize thermoelectric performance by controlling phase junctions through surface-ligand tuning.

Introduction

Thermoelectric materials can convert waste heat to electric energy without producing greenhouse gas emissions, thus attracting extensive interest over the past several decades.[1] The dimensionless figure of merit, $zT = S^2\sigma T/\kappa_{tot}$, is used to describe the performance of thermoelectric materials, where S is the Seebeck coefficient, σ is electrical conductivity, T is absolute working temperature, and κ_{tot} is the total thermal conductivity. Generally, κ_{tot} is composed of two parts, i.e., $\kappa_{tot} = \kappa_{ele} + \kappa_{lat}$, where κ_{ele} is the electronic thermal conductivity, and κ_{lat} is the lattice thermal conductivity.[2] Although there is a strong interdependence between the parameters S, σ, and κ_{tot}, the past years have witnessed continuous progress in improving zT through several rational design strategies such as modulation doping, matrix/precipitate band alignment, nanostructuring with second phases, and constructing all-scale hierarchical architectures.[3] For example, in the current state-of-the-art thermoelectric materials such as Bi_2Te_3,[4–6] GeTe,[7] PbTe,[8] and SnSe,[9–11] the peak zT values higher than 2.0 have been widely reported. Unfortunately, these materials usually contain expensive or toxic heavy elements, such as Ge, Se, Sb, Te, and Pb, which are undesirable for industrial applications. In contrast, eco-friendly and low-cost metallic sulfide-based thermoelectric materials have become great substitutes but have not yet achieved a $zT > 2$.[12]

Recently, phase engineering of nanomaterials (PEN), which assembles the conventional and unconventional phase domains, has achieved great success in various fields, including optics, electronics, photovoltaics, and catalysis, due to its capability of tuning physical properties via coupling and synergistic effects.[13] PEN enables great flexibility in modifying electronic and phononic structures and thus can potentially be utilized in thermoelectrics.[14] However, unconventional crystal polymorphism is rarely reported due to the instability of metastable phases under high working temperatures.

In this work, we utilize phase engineering in liquid-like $Cu_{2-x}S$-based thermoelectric materials, which have attracted tremendous interest due to the high abundance of Cu and S, low toxicity, tunable crystal polymorphs, and extraordinary thermoelectric properties.[12] We demonstrate a straightforward strategy to synthesize $Cu_{2-x}S$ phase-junction nanocomposites by retaining the surface 1-dodecanethiol (DDT) ligands, in contrast to the traditional method that strips the ligands. The DDT ligands retained on Cu_2S nanocrystal precursors can simultaneously tune the stoichiometry and the surface energy of $Cu_{2-x}S$ ($0 < x < 1$) nanocrystal solids. As a result, novel phase junctions between a conventional monoclinic phase and an unconventional metastable tetragonal phase are obtained. This strategy is referred to as a

[*] X. Li,[+] Y. Lou,[+] K. Jin, L. Fu, P. Xu, Prof. B. Xu
School of Chemistry and Chemical Engineering,
Nanjing University of Science and Technology
Nanjing, 210094 (P. R. China)
E-mail: louyue@njust.edu.cn
xubiao@njust.edu.cn

Prof. B. Xu
Chemical Engineering, Collaborative Innovation Center of Advanced Microstructures,
Nanjing University
Nanjing, 210093 (P. R. China)

Prof. Z. Shi
State Key Laboratory of Inorganic Synthesis and Preparative Chemistry, College of Chemistry,
Jilin University
Changchun, 130012 (P. R. China)

Dr. T. Feng
Department of Mechanical Engineering,
The University of Utah
Salt Lake City, UT 84112 (USA)

[+] These authors contributed equally to this work.

© 2022 Wiley-VCH GmbH

15213773, 2022, 45, Downloaded from https://onlinelibrary.wiley.com/doi/10.1002/anie.202212885 by University Of Utah, Wiley Online Library on [14/11/2022]. See the Terms and Conditions (https://onlinelibrary.wiley.com/terms-and-conditions) on Wiley Online Library for rules of use; OA articles are governed by the applicable Creative Commons License

ligand (decanethiol)-directed strategy. Density functional theory (DFT) calculations support that the DDT ligands retained on $Cu_{2-x}S$ nanocrystal precursors can effectively tune the stoichiometry and surface energy of $Cu_{2-x}S$. The t-phase $Cu_{1.96}S$ with high crystallographic symmetry improves the charge carrier effective mass (m^*). The copper vacancies (V_{Cu}) efficiently increase the carrier concentration (n_H). Moreover, the phase-junction interfaces induce a modulation doping effect, enhancing the carrier mobility (μ_H) and simultaneously increasing the phonon scattering and reducing κ_{lat}. As a result, the peak zT value of the phase-junction nanomaterials reaches 2.1 at 932 K, which is record-high among the $Cu_{2-x}S$ family and other metal sulfide compounds.

Results and Discussion

The critical challenges in the preparation of phase junctions lie in the precise control over the reaction kinetics and the underlying thermodynamics determined by multiple parameters, such as the stoichiometric ratio of Cu:S and the amount of surface-ligand capping. We addressed these challenges by tuning sulfur-containing ligands of colloidal nanocrystal precursors and the subsequent sintering assembly process, as illustrated in Figure 1 (details in the Methods section in Supporting Information). The Cu_2S nanoparticles with DDT ligands (19±3 nm, Figure S2a) were first prepared as powdered precursors. In the traditional solid-state approach, the Cu:S ratio was controlled by the feed ratio of elemental Cu and S.[15] This work innovatively prepared the monoclinic Cu_2S accompanied by the second tetragonal $Cu_{1.96}S$ phase by incorporating sulfur species from the surface ligands into Cu_2S, as illustrated by the following formula: $1.96\ Cu_2S + 0.04\ C_{12}H_{25}SH \rightarrow 2\,Cu_{1.96}S + 0.04\,C_{12}H_{26}$. This reaction took place simultaneously with the process of powder consolidation during spark plasma sintering (SPS). Inspired by the ability of heat-treatment to remove ligands,[16] the number of sulfur species from DDT ligands that participated in the reaction is regulated by the volatilization time of the samples under vacuum in a tube furnace before the SPS, resulting in phase junctions with different ratios of Cu_2S and $Cu_{1.96}S$ (Figure 1a, lower panel). In addition, the surface ligands bonding to the nanocrystals can also tune the surface energy[17] and grain size of nanocrystals. Due to the protection of DDT and/or inorganic carbon (Figure S1), a small grain size of 280± 45 nm is achieved (Figure S2c). As a comparison, the grain size is increased to 331±70 nm after the partial volatilization of the DDT ligand (Figure S2b).

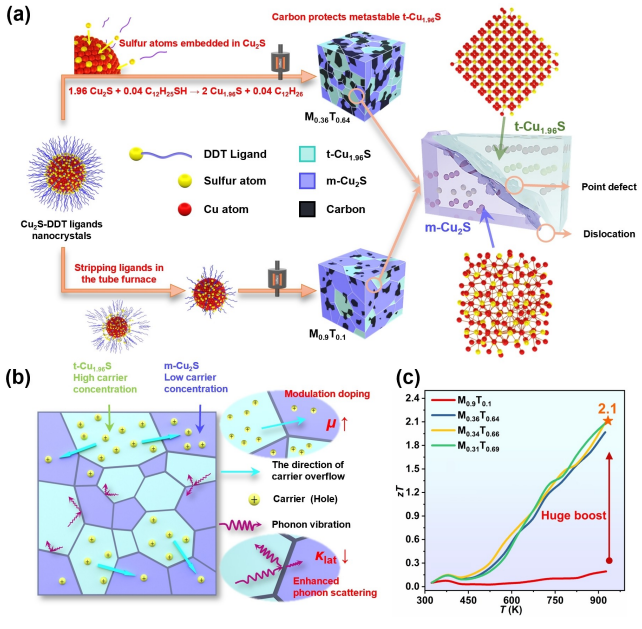

Figure 1. a) Schematic diagram of the surface ligand (decanethiol)-directed strategy for preparation of $Cu_{2-x}S$ nanomaterials with phase-junction interfaces between monoclinic and tetragonal phases. b) Illustration of the mechanism leading to the extraordinary thermoelectric properties. c) Comparison of zT of samples in this work.

Figure 2a presents the X-ray diffraction (XRD) pattern for copper sulfide with conventional monoclinic (JCPDS: 83-1462)[18] and metastable tetragonal phases (JCPDS: 29-0578).[19] Furthermore, Rietveld refinement[20] (Figure S4) confirms that the Cu_2S phase crystallizes in a monoclinic structure with a space group of $P2_1/c$ (a=15.246 Å, b=11.884 Å, c=13.494 Å).[18] In the monoclinic Cu_2S, all copper atoms are in triangular coordination with sulfur. Some Cu atoms are regular in bonding, and others show a pretty severe distortion in the triangle. The length of the Cu–S bond varies from 2.21 to 2.89 Å with an average of 2.33 Å.[21] As for tetragonal $Cu_{1.96}S$, its unit cell is $a=b$=3.996 Å, c=11.287 Å, belonging to the space group of $P4_32_12$.[19] Herein, Sulfur is located at the top of the triangular prism, surrounded by 12 Sulfur atoms at 3.99 Å and 6 Copper atoms at 2.31 Å. The significantly different bonding motifs between m-Cu_2S and t-$Cu_{1.96}S$ determine their different bulk and surface energies, as will be discussed afterward.[22]

Rietveld refinement revealed the molar ratio of m-Cu_2S to t-$Cu_{1.96}S$ was 0.36:0.64 in the SPSed Cu_2S nanocrystals sample, which is thus labeled as $M_{0.36}T_{0.64}$, standing for (m-Cu_2S)$_{0.36}$(t-$Cu_{1.96}S$)$_{0.64}$. The ratio of m-Cu_2S and t-$Cu_{1.96}S$ can be regulated by the tube furnace treatment time of the Cu_2S nanoparticles. When the duration of vacuum treatment is 3 h, the ratio of m-Cu_2S and t-$Cu_{1.96}S$ is 0.78:0.22 (Figure S4b). When the vacuum treatment is up to 12 h, the Cu_2S-rich sample (m-Cu_2S)$_{0.9}$(t-$Cu_{1.96}S$)$_{0.1}$ was obtained, labeled as $M_{0.9}T_{0.1}$. Apart from XRD analysis, the composition of our phase-junction samples can also be verified by Wavelength Dispersion Spectroscopy (WDS, Figure S3, and Table S1). They are determined to be 1.98±0.02 for $M_{0.36}T_{0.64}$ and 2.00±0.01 for $M_{0.9}T_{0.1}$. To further verify the successful regulation of phase junctions and the electronic structure of these two samples, X-ray absorption near-edge structure (XANES) and X-ray photoelectron spectroscopy (XPS) were performed. The XPS (Figure S6) shows that the binding energy of m-Cu_2S- t-$Cu_{1.96}S$ at the Cu 2p region could be divided into two peaks. For $M_{0.9}T_{0.1}$, the peaks at 952.2 eV and 932.3 eV are associated with Cu $2p_{1/2}$ and $2p_{3/2}$, respectively. $M_{0.36}T_{0.64}$ shows slightly higher Cu $2p_{1/2}$ and $2p_{3/2}$

© 2022 Wiley-VCH GmbH

15213773, 2022, 45, Downloaded from https://onlinelibrary.wiley.com/doi/10.1002/anie.202212885 by University Of Utah, Wiley Online Library on [14/11/2022]. See the Terms and Conditions (https://onlinelibrary.wiley.com/terms-and-conditions) on Wiley Online Library for rules of use; OA articles are governed by the applicable Creative Commons License

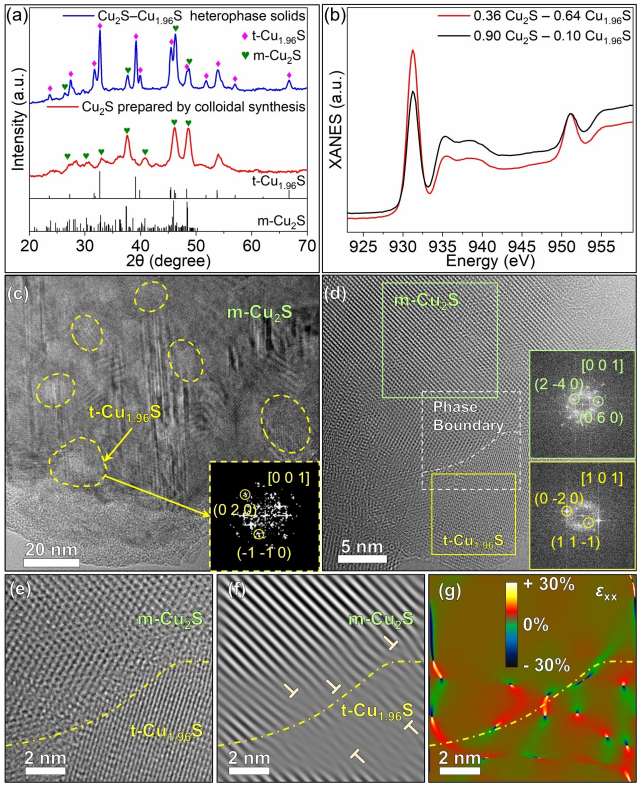

Figure 2. Crystal structure and morphology characterizations of as-obtained powder precursors and SPSed bulk samples. a) the X-ray diffraction (XRD) patterns of Cu_2S prepared by colloidal synthesis and Cu_2S–$Cu_{1.96}S$ phase-junction solids, b) Cu L-edge soft X-ray absorption near-edge spectroscopy (XANES) normalized spectra of $M_{0.36}T_{0.64}$ and $M_{0.9}T_{0.1}$, c) The Transmission Electron Microscopy (TEM) image of $M_{0.36}T_{0.64}$ sample with inserted the corresponding Fast Fourier Transform (FFT) patterns of the yellow dashed circles, d) the HRTEM image of t-$Cu_{1.96}S$ and m-Cu_2S in $M_{0.36}T_{0.64}$ sample with inserted the corresponding FFT pattern (the green and yellow boxes mark m-Cu_2S and t-$Cu_{1.96}S$ and their related FFT patterns, respectively), e) local zoom image of the white dotted box in (d), f) the corresponding IFFT pattern of (e) of adjacent grains crossing the phase boundary, and g) the geometric phase analysis (GPA) strain maps of ε_{xx} that correspond to the IFFT pattern of (e).

binding energy (952.4 eV and 932.5 eV), which implies a higher average valence state of Cu species in $M_{0.36}T_{0.64}$. This positive shift suggests that when more formation of t-$Cu_{1.96}S$ occurs, more proportion of Cu^{2+} than Cu^{+} in the m-Cu_2S- t-$Cu_{1.96}S$ phase junctions is achieved. Direct experimental evidence for the increased chemical valence of Cu was also obtained from XANES[23] (Figure 2b). The absorption peak (931.2 eV) of $M_{0.36}T_{0.64}$ exhibits a higher integral area than $M_{0.9}T_{0.1}$.

As shown in Figure 2c–g, the phase junctions of $M_{0.36}T_{0.64}$ are directly observed in TEM images. The t-$Cu_{1.96}S$ phase has a typical irregular morphology embedded inside the m-Cu_2S substrate (Figure 2c). On the one hand, an interfacial solid-phase reaction occurs between ≈19 nm Cu_2S nanoparticles and DDT ligands linked to the surface of nanoparticles. The S atoms in DDT are embedded in the surface of the Cu_2S nanoparticles to form localized t-$Cu_{1.96}S$ with smaller sizes (≈20 nm). On the other hand, consolidation of m-Cu_2S nanoparticles under high temperature and pressure leads to grain growth and a large grain of m-Cu_2S. The average sizes of m-Cu_2S grains observed from SEM images are ≈280 nm (Figure S2c).

The locally magnified TEM image of t-$Cu_{1.96}S$ and m-Cu_2S in Figure 2d and the corresponding Fast Fourier Transform (FFT) images are displayed. The FFT images clearly show the characteristic $P2_1/c$ [0 0 1] zone axis pattern of m-Cu_2S and characteristic $P4_32_12$ [1 0 1] of t-$Cu_{1.96}S$, respectively. The IFFT image (Figure 2f) of the phase boundary suggests that the phase interface contains many dislocations. The strain tensors, ε_{xx}, of two vertical diffraction spots were selected for geometric phase analysis (GPA, Figure 2g) to display the strain field of the phase boundary, which agrees with the significant dislocations at the phase interface.

Previous works have enhanced the thermoelectric properties of $Cu_{2-x}S$ by changing its stoichiometric ratio, such as Cu_2S, $Cu_{1.98}S$, $Cu_{1.97}S$, $Cu_{1.8}S$, etc.[24–27] However, the crystal structure of the $Cu_{2-x}S$ was still limited to the monoclinic phase, leading to limited optimization in thermoelectric performance. In this work, the monoclinic-tetragonal dual-phase structure has been achieved and stabilized using our ligand-assisted syntheses. To understand the underlying mechanism of the growth of dual-phase crystals and the formation of Cu vacancies, we have conducted DFT simulations. We have found that the Cu vacancy formation energies in various configurations of $Cu_{2-x}S$ with different x (Table S2) are relatively low and comparable to the room-temperature thermal fluctuation energy ($k_BT = 0.026$ eV), supporting that V_{Cu} can be easily generated at room temperature and that the as-obtained material is thermodynamically stable. In addition, according to the expression of the total energy of nanocrystals, $G = \frac{4}{3}\pi R^3 G_b + 4\pi R^2 \bar{\gamma}$, in which G_b is the volumetric bulk Gibbs free energy of formation, $\bar{\gamma}$ is the particle-averaged surface energy, and R is the particle size. The surface energy γ can account for a significant part of total energy when the grain size of nanocrystals is small.[28] Surface energies of different facets of the monoclinic and tetragonal phases are calculated and compared (Table S3). It is concluded that the bulk formation energy of the Cu vacancy-containing monoclinic phase is slightly lower, while the tetragonal phase has lower surface energy, which together forms a competitive monoclinic-tetragonal balance and finally establishes the mutual growth of m-Cu_2S and t-$Cu_{1.96}S$ in our phase-junction samples.

Thermoelectric properties of $M_{0.9}T_{0.1}$ and $M_{0.36}T_{0.64}$ from 323 to 923 K are shown in Figure 4. The electrical conductivity (σ) of $M_{0.9}T_{0.1}$ is lower than 1×10^3 S m^{-1}, which is close to the reported value of Cu_2S synthesized by the melting-annealing method.[29] In contrast, $M_{0.36}T_{0.64}$ shows a significantly higher σ, which is $\approx34.7\times10^3$ S m^{-1} at 324 K and increases to the maximum of $\approx62.2\times10^3$ S m^{-1} at 622 K and then declines to $\approx29.5\times10^3$ S m^{-1} at 923 K. Both samples exhibit p-type conduction (Figure 4e) with the hole concentrations n_H measured as 1.94×10^{19} and 48.9×10^{19} cm^{-3}, respectively, by using the Hall effect at room temperature

© 2022 Wiley-VCH GmbH

15213773, 2022, 45, Downloaded from https://onlinelibrary.wiley.com/doi/10.1002/anie.202212885 by University Of Utah, Wiley Online Library on [14/11/2022]. See the Terms and Conditions (https://onlinelibrary.wiley.com/terms-and-conditions) on Wiley Online Library for rules of use; OA articles are governed by the applicable Creative Commons License

(Figure 4b). This result indicates that the introduction of the V_{Cu}-containing t-phase plays a critical role in increasing the carrier concentration. More importantly, as shown in Figure 4c, the carrier mobility μ_H lifted from 2.6 $cm^2V^{-1}s^{-1}$ for $M_{0.9}T_{0.1}$ to 4.5 $m^2V^{-1}s^{-1}$ for $M_{0.36}T_{0.64}$ is a result of modulation doping. To have a qualitative analysis of the charge carrier redistribution between the t-$Cu_{1.96}S$ phase and m-Cu_2S phase grains, a simplified model based on DFT calculation results (Figure 3) is proposed (Figure S18). For our p-type materials design, the t-$Cu_{1.96}S$ phase nanoparticles have relatively higher valence band edges than the m-Cu_2S phase grains, forcing the carriers to flow into the matrix.[3,30,31] Holes can spill over from t-$Cu_{1.96}S$ grains into the m-Cu_2S grains with much-reduced impurity scattering, thereby increasing the hole mobility of $M_{0.36}T_{0.64}$. Therefore, besides the enhanced n_H, the μ_H increases simultaneously, leading to increased σ, further proving the advantage of our materials designing approach. At the same time, however, the Seebeck coefficient (Figure 4e) decreased from 269 $\mu V K^{-1}$ to 62 $\mu V K^{-1}$ (at room temperature), probably due to the increase of n_H since $S = \frac{8\pi^2k^2}{3eh^2}m^*T\left(\frac{\pi}{3n}\right)^{2/3}$, where S is inversely proportional to $n_H^{2/3}$. Since S is proportional to the effective mass (m^*), we measured m^* by the Pisarenko plot,[32] as shown in Figure 4d. m^* slightly improved from $M_{0.9}T_{0.1}$ (1.61 m_e) to $M_{0.36}T_{0.64}$ (1.74 m_e), where m_e is the free electron mass. Despite the reduction of S, the significantly improved electrical conductivity still pushes the power factor of $M_{0.36}T_{0.64}$ to be much higher than $M_{0.9}T_{0.1}$ (Figure 4f), demonstrating the effectiveness of electrical transport modulation by the phase-junction nanocomposites.

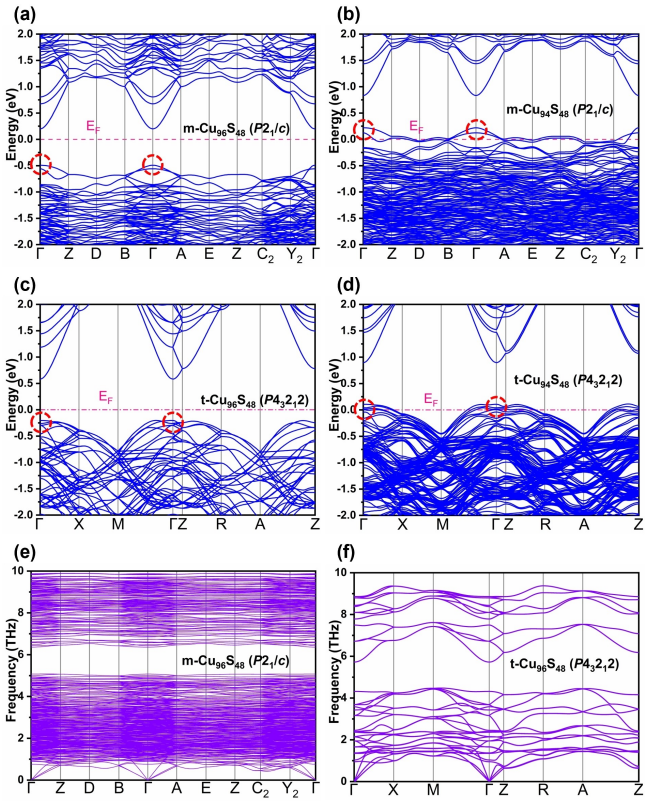

Figure 3. a) GGA + U calculated the electronic band structure of a) V_{Cu}-free m-Cu_2S (m-$Cu_{96}S_{48}$) with $P2_1/c$ space group, b) m-Cu_2S with $2V_{Cu}$ (m-$Cu_{94}S_{48}$), c) V_{Cu}-free t-$Cu_{1.96}S$ (t-$Cu_{96}S_{48}$) with $P4_32_12$ space group, and d) t-$Cu_{1.96}S$ with $2V_{Cu}$ (t-$Cu_{94}S_{48}$). (Broken red circles mark Γ points) The phonon dispersions of e) m-$Cu_{96}S_{48}$ and f) t-$Cu_{96}S_{48}$.

From $M_{0.9}T_{0.1}$ to $M_{0.36}T_{0.64}$, accompanied by the increase of power factor, the thermal conductivity is also increased—from about 0.5 $W m^{-1}K^{-1}$ to 0.7 $W m^{-1}K^{-1}$, as shown in Figure 4g. This increase is mainly contributed by electrons since the latter has a much higher electrical conductivity. According to the Wiedemann-Franz law, the electronic thermal conductivity $\kappa_{ele} = L\sigma T$ is proportional to σ, where $L = (1.5 + \exp(-|S|/116)) \times 10^{-8}$) is the Lorenz number.[33] By subtracting κ_{ele} from κ_{tot}, we estimated κ_{lat} (Figure 4h). It is found that, despite the increase in total thermal conductivity, the lattice contribution is decreased significantly. For example, at 923 K, κ_{lat} of $M_{0.36}T_{0.64}$ is about 0.17 $W m^{-1}K^{-1}$, which is much lower than the 0.52 $W m^{-1}K^{-1}$ of $M_{0.9}T_{0.1}$. The decreased κ_{lat} with increasing content of the t-phase might be the increased density of grain boundaries and phase interfaces (Figure S2b, c).[3] In addition, the presence of point defects (V_{Cu}) and mesoscale carbon-inorganic interface could also scatter phonons with different frequencies and decrease the lattice thermal conductivity. The phenomenon that the κ_{lat} does not decrease with increasing temperature for both samples in the high-temperature region might be because of two reasons. First, the phonon mean free path can gradually approach its minimum value due to high-temperature anharmonic phonon scattering, phonon-defect, and phonon-grain boundary scattering (Figure 2c). Therefore, in the high-temperature region, the thermal conductivity does not decrease significantly with increasing temperature. Second, the anharmonic force constants and the phonon scattering cross-section might be softened at high temperatures, which can slow down or even flip the decreasing trend of thermal conductivity with temperature.[34,35] After the second phase-transition point (720 to 930 K), the monoclinic ($M_{0.9}T_{0.1}$) phase shows an increased κ_{lat} when increasing temperature. This is possibly induced by bipolar thermal conductivity.[36]

Combining the power factor and thermal conductivity, the zT values of $M_{0.9}T_{0.1}$ to $M_{0.36}T_{0.64}$ are calculated and shown in Figure 4 i. The latter increases significantly with temperature and reaches the maximum of 2.0 at the maximum temperature of 923 K. In contrast, $M_{0.9}T_{0.1}$, with little phase-junction interface, shows a substantially lower zT of <0.2 throughout the temperature range. This result demonstrates the effectiveness of phase-junction interface engineering in developing new thermoelectric materials. Additionally, results obtained from $M_{0.36}T_{0.64}$ showed good repeatability across various samples (Figure 4i), where the error bar data were obtained from three different experimental batches. In addition, we measured the thermoelectric properties of $M_{0.36}T_{0.64}$ in two perpendicular directions (Figure S12) and found no obvious anisotropy.

To better understand the electrical transport properties of $M_{0.9}T_{0.1}$ and $M_{0.36}T_{0.64}$, we calculated the band structures and density of states (DOS) of m-$Cu_{96}S_{48}$, m-$Cu_{95}S_{48}$, m-$Cu_{94}S_{48}$, t-$Cu_{96}S_{48}$, t-$Cu_{95}S_{48}$, and t-$Cu_{94}S_{48}$ by DFT, as shown

© 2022 Wiley-VCH GmbH

15213773, 2022, 45, Downloaded from https://onlinelibrary.wiley.com/doi/10.1002/anie.202212885 by University Of Utah, Wiley Online Library on [14/11/2022]. See the Terms and Conditions (https://onlinelibrary.wiley.com/terms-and-conditions) on Wiley Online Library for rules of use; OA articles are governed by the applicable Creative Commons License

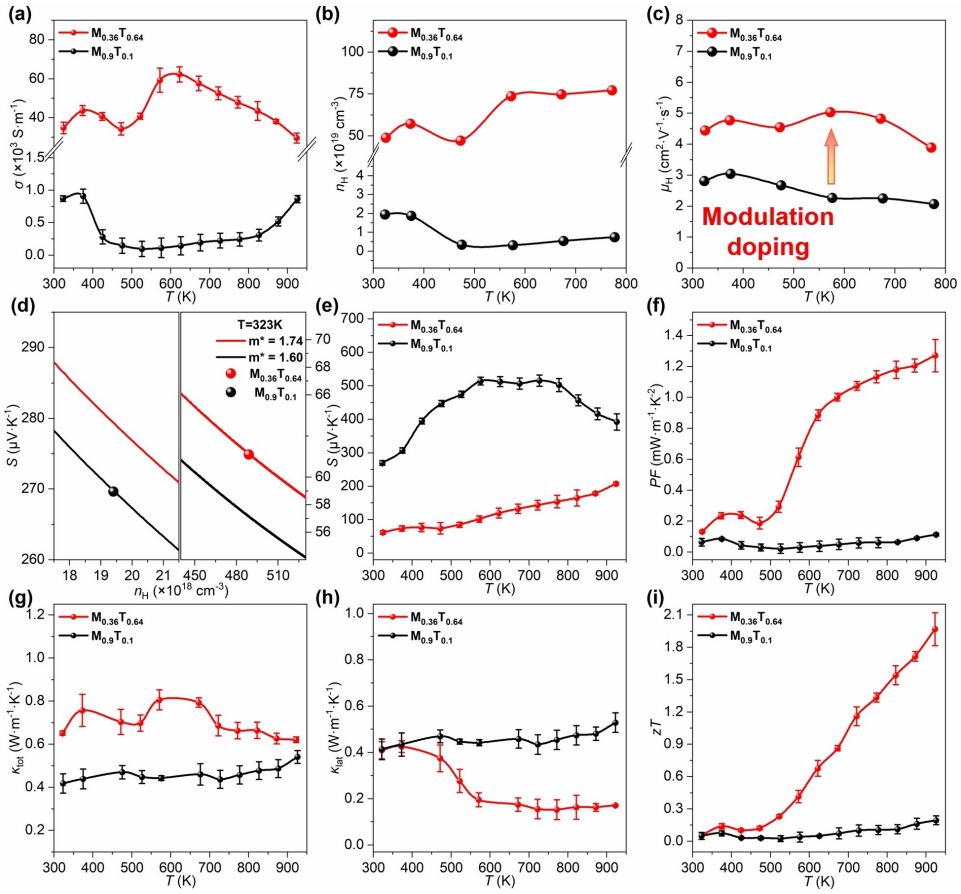

Figure 4. Thermoelectric properties of the $M_{0.36}T_{0.64}$ and $M_{0.9}T_{0.1}$ samples: T-dependent a) σ, b) n_H, and c) μ_H, d) S as a function of experimental n_H, e) S, f) PF, g) κ_{tot}, h) κ_{lat}, and i) zT.

in Figure 3 and Figure S8. Generalized gradient approximation (GGA) with a Hubbard U[37,38] is used. All six simulations show direct band gaps with the conduction band minimum (CBM) and valence band maximum (VBM) located at the Γ point (broken red circles in Figure 3a–d). The simulations with Cu vacancies show Fermi levels inside the valence bands, indicating degenerate p-type semiconductors with large carrier concentrations. This explains why increasing t-phase content can significantly increase the hole concentration and electrical conductivity. Based on the band structures, the *m*-phase and t-phase can be viewed as undoped and highly-doped semiconductors. Their phase-junction structure can possibly form band offsets. Thus, the experimentally observed hole mobility increase of $M_{0.36}T_{0.64}$ compared to $M_{0.9}T_{0.1}$ might be because of modulation doping. Since the heterostructure is hard to construct and may contain an amorphous intermediate layer, as shown in the TEM image in Figure 2e, it exceeds the DFT simulation capability. In addition, we have also calculated the density-of-states effective mass (m_d*), and t-$Cu_{1.96}S$ is found to be higher than m-Cu_2S (Table S4), which also agrees with the experimental trend.

To better understand phonon and thermal properties, we calculated the phonon dispersion relations of monoclinic and tetragonal phases using density functional perturbation theory (DFPT), as shown in Figure 3e, f. The phonon dispersion of the tetragonal phase does not show any imaginary frequencies, indicating that the structure is locally stable. According to the kinetic theory, the lattice thermal conductivity is $\kappa_{lat,z} = \frac{1}{NV}\sum_\lambda (v_\lambda \cdot \hat{z})^2 c_\lambda \tau_\lambda$, where $\hat{z}$ is the transport direction, λ is the shorthand of phonon mode ($\mathbf{k}$, v) with $\mathbf{k}$ representing the phonon wave vector and v labeling the phonon dispersion branch, V is the volume of a primitive cell, N is the number of $\mathbf{k}$ points, and the summation is done over all phonon modes. The specific heat per mode is $c_\lambda = \hbar\omega_\lambda \partial n_\lambda^0/\partial T = k_B x^2 e^x/(e^x-1)^2$, where n_λ^0 is phonon occupation number of the Bose-Einstein distribution $n_\lambda^0 = (e^x-1)^{-1}$, x is the shorthand of $\hbar\omega_\lambda/k_B T$, and k_B is Boltzmann constant.[34,39,40]

Overall, the phonon group velocity, v, of the tetragonal phase is larger than that of the monoclinic phase, and the phonon heat capacities of the two phases are similar (Figure S13). Based on the comparison of experimental κ_{lat} and calculated $\kappa_z = \frac{1}{NV}\sum_\lambda (v_\lambda \cdot \hat{z})^2 c_\lambda \tau_\lambda$ (Table S5, 6), we conclude that the relaxation time of the tetragonal phase should be much lower than that of the monoclinic phase in the experimental samples. This is supported by the TEM of $M_{0.36}T_{0.64}$ (Figure 2c), where the tetragonal phase is dispersed in the monoclinic phase with much smaller grains on the nanoscale. As a result, the material with more tetragonal

© 2022 Wiley-VCH GmbH

15213773, 2022, 45, Downloaded from https://onlinelibrary.wiley.com/doi/10.1002/anie.202212885 by University Of Utah, Wiley Online Library on [14/11/2022]. See the Terms and Conditions (https://onlinelibrary.wiley.com/terms-and-conditions) on Wiley Online Library for rules of use; OA articles are governed by the applicable Creative Commons License

phase nanograins ($M_{0.36}T_{0.64}$) exhibits lower thermal conductivity due to abundant grain boundaries and tetragonal nanograins scattering on phonon.

Stimulated by the promising thermoelectric performance of $M_{0.36}T_{0.64}$, we further increase the phase-junction content of the t-phase via surface engineering. Two strategies are explored. The first strategy is to expose the as-obtained Cu_2S to ambient air for five days, and the second strategy is to mix the as-synthesized Cu_2S with oleylamine (OAm) for 60 minutes and then expose it to ambient air for five days. In the first strategy, copper vacancies are formed in stoichiometric Cu_2S via surface oxidation by the ambient air, resulting in copper-deficient $Cu_{2-x}S$ phases, which are mainly djurleite ($Cu_{1.96}S$):[41–43] $Cu_2S + O_2 \rightarrow Cu_{1.96}S + Cu_2O$. Therefore, we intentionally exposed as-obtained Cu_2S to ambient air for five days to obtain a higher fraction of $Cu_{1.96}S$ in the dual-phase nanocomposite. In the second strategy, the surface ligands can further affect the surface reaction and tune the stoichiometry of Cu: S. Therefore, we mixed the as-obtained Cu_2S and OAm followed by stirring at 50 °C. During this reaction process, the Cu^+ ions in Cu_2S are dissolved in OAm, resulting in the Cu^+-OAm complex, which may be further oxidized as Cu^{2+}-OAm by the air.[44] The characteristic blue color observed in the reaction solution supports the desolvation of Cu. This way, more Cu^+ could be removed from Cu_2S, and more $Cu_{1.96}S$ can be produced.

Rietveld refinement of the XRD spectra shows that the ratio of the m to t-phases is 0.34:0.66 and 0.31:0.69 for the two treatments, respectively. Thus, the two samples are labeled $M_{0.34}T_{0.66}$ and $M_{0.31}T_{0.69}$, respectively (Figure S4d, e). As expected, both post-treatment methods can increase the content of the t-phase. In addition, the surface oxidation and ligand extraction of Cu^+ could lead to more t-$Cu_{1.96}S$ and further increase the valence state of Cu, which is proved by the XPS spectrum of samples (Figure S6). $M_{0.34}T_{0.66}$ and $M_{0.31}T_{0.69}$ show the chemical state of Cu $2p_{1/2}$ with higher binding energy (952.5 eV and 952.6 eV, respectively) than that of $M_{0.36}T_{0.64}$ (952.3 eV), demonstrating that the average valence state of Cu species is increased. In addition, the appearance of the O spectrum (Figure S7) and the absence of the Cu^{2+} satellite peak at 961.9 eV imply that the oxide of copper exists in the form of Cu_2O. By calculating the peak areas of the different elements in the XPS of $M_{0.34}T_{0.66}$ and $M_{0.31}T_{0.69}$, the proportion of Cu_2O is identified as 0.40 wt % in $M_{0.34}T_{0.66}$ and 0.53 wt % in $M_{0.31}T_{0.69}$, respectively (Figure S17).

Subsequently, thermoelectric performances were measured. The temperature-dependent electrical conductivity is shown in Figure 5a. Interestingly, it is found that σ is

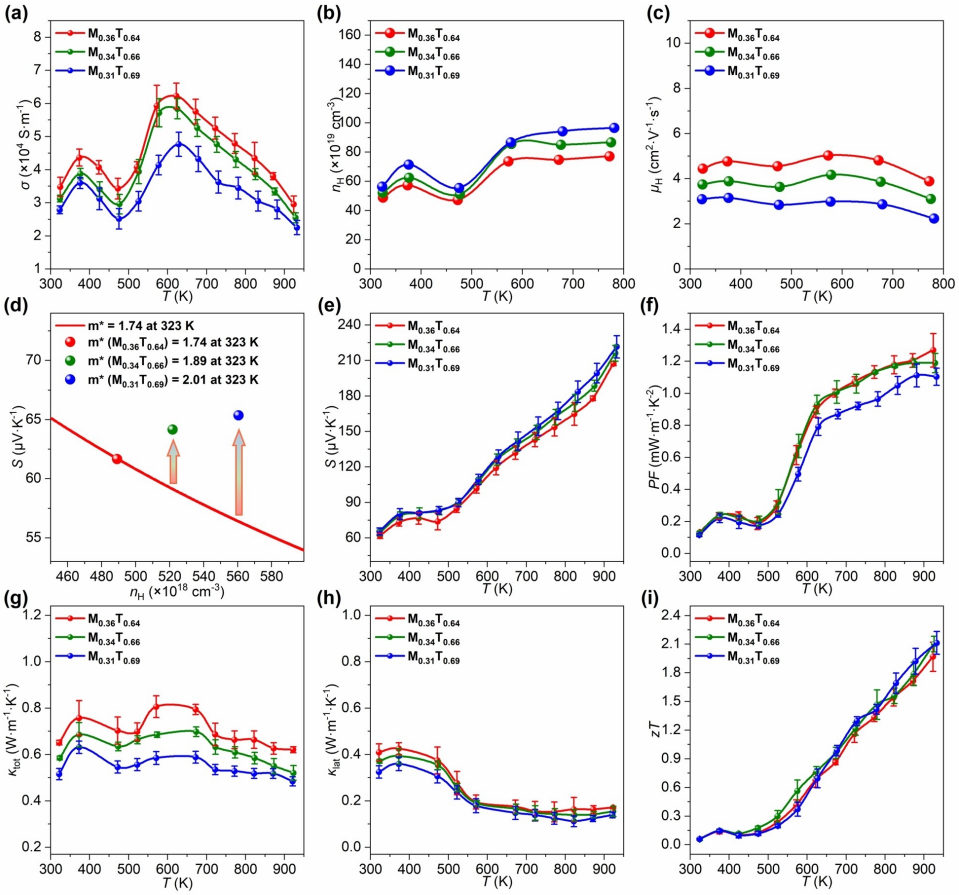

Figure 5. Thermoelectric properties of the $M_{0.36}T_{0.64}$, $M_{0.34}T_{0.66}$, and $M_{0.31}T_{0.69}$ samples: T-dependent a) σ, b) n_H, and c) μ_H, d) S as a function of experimental n_H, e) S, f) PF, g) κ_{tot}, h) κ_{lat}, and i) zT.

© 2022 Wiley-VCH GmbH

15213773, 2022, 45, Downloaded from https://onlinelibrary.wiley.com/doi/10.1002/anie.202212885 by University Of Utah, Wiley Online Library on [14/11/2022]. See the Terms and Conditions (https://onlinelibrary.wiley.com/terms-and-conditions) on Wiley Online Library for rules of use; OA articles are governed by the applicable Creative Commons License

decreased when the t-phase content is further increased. For example, the room temperature σ values are 3.4, 3.1, and 2.7×10^4 S m^{-1} for $M_{0.36}T_{0.64}$, $M_{0.34}T_{0.66}$, and $M_{0.31}T_{0.69}$, respectively. This could be attributed to the introduction of Cu_2O and V_{Cu} in the latter two samples. Although the increase of V_{Cu} slightly increases the carrier concentrations (Figure 5b), the Cu_2O by air oxidation can provide scattering to charge carriers and reduce carrier mobility μ_H (Figure 5c), thus decreasing σ. Accompanied by the decrease of σ, S increases (Figure 5e). The improved S (Figure 5e) of the $M_{0.34}T_{0.66}$ and $M_{0.31}T_{0.69}$ samples may be caused by the high potential barrier (E_{Bn}) value originating from the grain boundaries. We infer that Cu_2O at the grain boundaries may increase E_{Bn} at the boundaries and selectively scatter low-energy carriers, increasing S.[45,46] The decreased σ and slightly enhanced S of the $M_{0.34}T_{0.66}$ and $M_{0.31}T_{0.69}$ slightly reduce their PF (Figure 5f).

The thermal conductivity is also reduced (Figure 5g) with increasing content of the t-phase. For example, $M_{0.36}T_{0.64}$ and $M_{0.31}T_{0.69}$ show lower κ_{tot} (0.58 W m^{-1} K^{-1} and 0.51 W m^{-1} K^{-1}) at room temperature and minima (0.52 W m^{-1} K^{-1} and 0.48 W m^{-1} K^{-1}) at ≈923 K. We have also extracted κ_{lat} (Figure 5h), which shows a slight decrease with increasing content of the t-phase as well. The three samples have the same trends of κ_{tot} -T throughout the temperature range. The $M_{0.31}T_{0.69}$ has the minimum κ_{lat} value of 0.14 W m^{-1} K^{-1} at 923 K. Because of the relatively small grain size of the t-phase (Figure 2c), its increased content results in an increase in the phase-junction interface density, which effectively scatters phonons. Introducing Cu_2O will also enhance phonons scattering, reducing the κ_{lat}. In addition, the increased point defects (V_{Cu}) can also help reduce κ_{lat}.

Due to the slightly reduced PF and much-reduced κ_{tot}, a record high zT_{max} of 2.1 (at 932 K) is achieved for $M_{0.31}T_{0.69}$ (Figure 5i), where the error bar data are deduced from three batches of pellets. Figure 6 compares the zT values achieved in this work with the state-of-the-art peak zT in $Cu_{2-x}S$-based compounds and other metal sulfide families, indicating that the thermoelectric performance of this work is record-high.

We note that thermal and electrical stabilities are critical issues in copper-chalcogenide thermoelectric materials. As evidenced by TGA (Figure S9), the as-synthesized $Cu_{2-x}S$-based phase-junction materials exhibit good thermal stability up to 923 K. Moreover, XRD patterns of samples after the cycling test (Figure S10) demonstrated the structural stability of metastable tetragonal phase and m-Cu_2S-t-$Cu_{1.96}S$ phase junctions, which did not show any degradation or precipitation of copper. At the same time, the statistical analysis of particle size (Figure S2e, f) showed no significant change in grain size after three cyclic tests. Furthermore, the Seebeck coefficient, the electrical resistivity, and the power factor remained almost unchanged after the cycling test (Figure S11). This thermal stability is attributed to the surface ligands of DDT and OAm used in the solution synthesis. During the SPS process, these ligands were carbonized into carbon and coated on the grain of $Cu_{2-x}S$ (Figure S1). Meanwhile, the interface energy barrier between m- and t- phases may hinder the diffusion of Cu^+ ions, leading to the high stability of our samples.

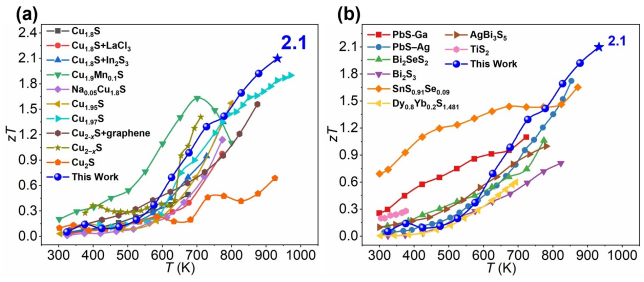

Figure 6. a) zT of $Cu_{2-x}S$-base thermoelectric materials[15,22,26,27,47–52] and b) the comparison with other metal sulfide compounds taken from the literature.[53–60]

Conclusion

A surface ligand (decanethiol)-directed strategy is developed to synthesize controlled monoclinic Cu_2S-tetragonal $Cu_{1.96}S$ phase-junction nanocomposites, whose phase composition can be tuned by surface oxidation and cation exchange. The increased content of the tetragonal phase significantly increases the carrier concentrations and electrical transport. At the same time, it increases the density of phase-junction interfaces and the phonon scattering, resulting in largely decreased thermal conductivity. As a result, a record-high zT value of 2.11 is achieved at ≈923 K in the $(m\text{-}Cu_2S)_{0.31}(t\text{-}Cu_{1.96}S)_{0.69}$ samples. Our work demonstrates that phase-junction engineering can be an effective strategy for developing high-performance thermoelectric materials. The charge redistribution at the phase junctions and the suppressed thermal transport may also shed light on many other research communities, as exemplified by electronic devices and thermal management.

Acknowledgements

B.X. thanks financial support from 1000 young talents, Innovation and Entrepreneurship Talents in Jiangsu Province, Key Laboratory for Soft Chemistry and Functional Materials of Ministry of Education, Nanjing University of Science and Technology, and State Key Laboratory of Coordination Chemistry, School of Chemistry and Chemical Engineering, Nanjing University. Y.L. thanks financial support from the Doctor of Entrepreneurship and Innovation in Jiangsu Province (JSSCBS20210215).

Conflict of Interest

The authors declare no conflict of interest.

© 2022 Wiley-VCH GmbH

15213773, 2022, 45, Downloaded from https://onlinelibrary.wiley.com/doi/10.1002/anie.202212885 by University Of Utah, Wiley Online Library on [14/11/2022]. See the Terms and Conditions (https://onlinelibrary.wiley.com/terms-and-conditions) on Wiley Online Library for rules of use; OA articles are governed by the applicable Creative Commons License

Data Availability Statement

The data that support the findings of this study are available from the corresponding author upon reasonable request.

Keywords: $Cu_{2-x}S$ · Metastable Phase · Phase Junctions · Polymorph · Thermoelectrics

[1] B. Xu, M. T. Agne, T. Feng, T. C. Chasapis, X. Ruan, Y. Zhou, H. Zheng, J. H. Bahk, M. G. Kanatzidis, G. J. Snyder, Y. Wu, *Adv. Mater.* **2017**, *29*, 1605140.
[2] X. L. Shi, J. Zou, Z. G. Chen, *Chem. Rev.* **2020**, *120*, 7399–7515.
[3] G. Tan, L. D. Zhao, M. G. Kanatzidis, *Chem. Rev.* **2016**, *116*, 12123–12149.
[4] L. P. Hu, T. J. Zhu, Y. G. Wang, H. H. Xie, Z. J. Xu, X. B. Zhao, *NPG Asia Mater.* **2014**, *6*, e88.
[5] C. L. Chen, T. H. Wang, Z. G. Yu, Y. Hutabalian, R. K. Vankayala, C. C. Chen, W. P. Hsieh, H. T. Jeng, D. H. Wei, Y. Y. Chen, *Adv. Sci.* **2022**, *9*, 2201353.
[6] S. I. Kim, H. K. Lee, H. A. Mun, H. S. Kim, S. W. Hwang, W. J. Roh, J. D. Yang, H. W. Shin, S. X. Li, H. Y. Lee, G. J. Snyder, W. S. Kim, *Science* **2015**, *348*, 109–114.
[7] M. Hong, Z. G. Chen, L. Yang, Y. C. Zou, M. S. Dargusch, H. Wang, J. Zou, *Adv. Mater.* **2018**, *30*, 1705942.
[8] H. J. Wu, L. D. Zhao, F. S. Zheng, D. Wu, Y. L. Pei, X. Tong, M. G. Kanatzidis, J. Q. He, *Nat. Commun.* **2014**, *5*, 4515.
[9] L. D. Zhao, S. H. Lo, Y. Zhang, H. Sun, G. Tan, C. Uher, C. Wolverton, V. P. Dravid, M. G. Kanatzidis, *Nature* **2014**, *508*, 373–377.
[10] C. Chang, M. Wu, D. He, Y. Pei, C. F. Wu, X. Wu, H. Yu, F. Zhu, K. Wang, Y. Chen, L. Huang, J. F. Li, J. He, L. D. Zhao, *Science* **2018**, *360*, 778–783.
[11] C. Zhou, Y. K. Lee, Y. Yu, S. Byun, Z. Z. Luo, H. Lee, B. Ge, Y. L. Lee, X. Chen, J. Y. Lee, O. Cojocaru-Miredin, H. Chang, J. Im, S. P. Cho, M. Wuttig, V. P. Dravid, M. G. Kanatzidis, I. Chung, *Nat. Mater.* **2021**, *20*, 1378–1384.
[12] W. D. Liu, L. Yang, Z. G. Chen, J. Zou, *Adv. Mater.* **2020**, *32*, 1905703.
[13] Y. Chen, Z. Lai, X. Zhang, Z. Fan, Q. He, C. Tan, H. Zhang, *Nat. Chem. Rev.* **2020**, *4*, 243–256.
[14] S. Gemming, T. Kunze, K. Morawetz, V. Pankoke, R. Luschtinetz, G. Seifert, *Eur. Phys. J. Spec. Top.* **2009**, *177*, 83–101.
[15] Y. Yu, D. Yang, J. Li, M. Zhang, H. Luo, Q. Liang, H. Ye, Q. Zhang, X. Tang, J. Wu, *Adv. Funct. Mater.* **2022**, *32*, 2107284.
[16] Q. Zhang, J.-B. Joo, Z. Lu, M. Dahl, D. Q. L. Oliveira, M. Ye, Y. Yin, *Nano Res.* **2011**, *4*, 103–114.
[17] F.-J. Fan, L. Wu, S.-H. Yu, *Energy Environ. Sci.* **2014**, *7*, 190–208.
[18] H. T. Evans, *Nat. Phys. Sci.* **1971**, *232*, 69–70.
[19] A. Janosi, *Acta Crystallogr.* **1964**, *17*, 311–312.
[20] B. H. Toby, *J. Appl. Crystallogr.* **2001**, *34*, 210–213.
[21] P. Lemoine, G. Guelou, B. Raveau, E. Guilmeau, *Angew. Chem. Int. Ed.* **2022**, *61*, e202108686; *Angew. Chem.* **2022**, *134*, e202108686.
[22] M. Li, Y. Liu, Y. Zhang, X. Han, T. Zhang, Y. Zuo, C. Xie, K. Xiao, J. Arbiol, J. Llorca, M. Ibanez, J. Liu, A. Cabot, *ACS Nano* **2021**, *15*, 4967–4978.
[23] B. Srinivasan, S. Cui, C. Prestipino, A. Gellé, C. Boussard-Pledel, S. Ababou-Girard, A. Trapananti, B. Bureau, S. Di Matteo, *J. Phys. Chem. C* **2017**, *121*, 14045–14050.
[24] Y. He, T. Day, T. Zhang, H. Liu, X. Shi, L. Chen, G. J. Snyder, *Adv. Mater.* **2014**, *26*, 3974–3978.
[25] Y. Yao, B.-P. Zhang, J. Pei, Y.-C. Liu, J.-F. Li, *J. Mater. Chem. C* **2017**, *5*, 7845–7852.
[26] Z.-H. Ge, Y.-X. Zhang, D. Song, X. Chong, P. Qin, F. Zheng, J. Feng, L.-D. Zhao, *J. Mater. Chem. A* **2018**, *6*, 14440–14448.
[27] P. Nieroda, J. Leszczynski, A. Mikula, K. Mars, M. J. Kruszewski, A. Kolezynski, *Ceram. Int.* **2020**, *46*, 25460–25466.
[28] D. A. Kitchaev, G. Ceder, *Nat. Commun.* **2016**, *7*, 13799.
[29] H. Luo, D. W. Yang, Y. M. Yu, Q. Liang, H. Y. Peng, F. J. Xia, X. F. Tang, J. S. Wu, *Adv. Electron. Mater.* **2022**, *8*, 2100835.
[30] T. O. Poehler, D. Abraham, *Appl. Phys. Lett.* **1965**, *6*, 125–126.
[31] M. Zebarjadi, G. Joshi, G. Zhu, B. Yu, A. Minnich, Y. Lan, X. Wang, M. Dresselhaus, Z. Ren, G. Chen, *Nano Lett.* **2011**, *11*, 2225–2230.
[32] L. Hu, Y. Luo, Y. W. Fang, F. Qin, X. Cao, H. Xie, J. Liu, J. Dong, A. Sanson, M. Giarola, X. Tan, Y. Zheng, A. Suwardi, Y. Huang, K. Hippalgaonkar, J. He, W. Zhang, J. Xu, Q. Yan, M. G. Kanatzidis, *Adv. Energy Mater.* **2021**, *11*, 2100661.
[33] L. Yang, Z. G. Chen, M. Hong, L. H. Wang, D. L. Kong, L. Q. Huang, G. Han, Y. C. Zou, M. Dargusch, J. Zou, *Nano Energy* **2017**, *31*, 105–112.
[34] T. L. Feng, L. Lindsay, X. L. Ruan, *Phys. Rev. B* **2017**, *96*, 161201.
[35] X. Yang, J. Tiwari, T. Feng, *Mater. Today Phys.* **2022**, *24*, 100689.
[36] V. M. Glazov, A. S. Burkhanov, *High Temp.* **1985**, *23*, 707–711.
[37] S. K. Barman, M. N. Huda, *J. Phys. Condens. Matter* **2018**, *30*, 165701.
[38] S. K. Barman, M. N. Huda, *J. Appl. Phys.* **2020**, *128*, 015703.
[39] L. Lindsay, D. A. Broido, N. Mingo, *Phys. Rev. B* **2010**, *82*, 115427.
[40] T. Feng, X. Ruan, *J. Nanomater.* **2014**, *2014*, 206370.
[41] S. G. Ellis, *J. Appl. Phys.* **1967**, *38*, 2906–2912.
[42] A. Putnis, *Philos. Mag.* **1976**, *34*, 1083–1086.
[43] J. M. Luther, P. K. Jain, T. Ewers, A. P. Alivisatos, *Nat. Mater.* **2011**, *10*, 361–366.
[44] R. Shen, W. Chen, Q. Peng, S. Lu, L. Zheng, X. Cao, Y. Wang, W. Zhu, J. Zhang, Z. Zhuang, C. Chen, D. Wang, Y. Li, *Chem* **2019**, *5*, 2099–2110.
[45] C. Hu, K. Xia, C. Fu, X. Zhao, T. Zhu, *Energy Environ. Sci.* **2022**, *15*, 1406–1422.
[46] K. Kishimoto, M. Tsukamoto, T. Koyanagi, *J. Appl. Phys.* **2002**, *92*, 5331–5339.
[47] L. Zhao, X. Wang, F. Y. Fei, J. Wang, Z. Cheng, S. Dou, J. Wang, G. J. Snyder, *J. Mater. Chem. A* **2015**, *3*, 9432–9437.
[48] H. C. Tang, F. H. Sun, J. F. Dong, Asfandiyar, H. L. Zhuang, Y. Pan, J. F. Li, *Nano Energy* **2018**, *49*, 267–273.
[49] Z. H. Ge, X. Chong, D. Feng, Y. X. Zhang, Y. Qiu, L. Xie, P. W. Guan, J. Feng, J. He, *Mater. Today Phys.* **2019**, *8*, 71–77.
[50] D. S. Nkemeni, Z. Yang, S. Y. Lou, G. H. Li, S. M. Zhou, *J. Alloys Compd.* **2021**, *878*, 160128.
[51] Z.-H. Ge, X. Liu, D. Feng, J. Lin, J. He, *Adv. Energy Mater.* **2016**, *6*, 1600607.
[52] Z.-H. Ge, B. P. Zhang, Y. X. Chen, Z. X. Yu, Y. Liu, J. F. Li, *Chem. Commun.* **2011**, *47*, 12697–12699.
[53] C. Wan, X. Gu, F. Dang, T. Itoh, Y. Wang, H. Sasaki, M. Kondo, K. Koga, K. Yabuki, G. J. Snyder, R. Yang, K. Koumoto, *Nat. Mater.* **2015**, *14*, 622–627.
[54] M. Ibanez, Z. Luo, A. Genc, L. Piveteau, S. Ortega, D. Cadavid, O. Dobrozhan, Y. Liu, M. Nachtegaal, M. Zebarjadi, J. Arbiol, M. V. Kovalenko, A. Cabot, *Nat. Commun.* **2016**, *7*, 10766.
[55] G. Tan, S. Hao, J. Zhao, C. Wolverton, M. G. Kanatzidis, *J. Am. Chem. Soc.* **2017**, *139*, 6467–6473.
[56] W. He, D. Wang, H. Wu, Y. Xiao, Y. Zhang, D. He, Y. Feng, Y.-J. Hao, J.-F. Dong, R. Chetty, L. Hao, D. Chen, J. Qin, Q. Yang, X. Li, J.-M. Song, Y. Zhu, W. Xu, C. Niu, X. Li, G.

© 2022 Wiley-VCH GmbH

15213773, 2022, 45, Downloaded from https://onlinelibrary.wiley.com/doi/10.1002/anie.202212885 by University Of Utah, Wiley Online Library on [14/11/2022]. See the Terms and Conditions (https://onlinelibrary.wiley.com/terms-and-conditions) on Wiley Online Library for rules of use; OA articles are governed by the applicable Creative Commons License

Wang, C. Liu, M. Ohta, J. Pennycook Stephen, J. He, J.-F. Li, L.-D. Zhao, *Science* **2019**, *365*, 1418–1424.
[57] R. Cheng, D. Y. Wang, H. Bai, J. S. Wu, W. Liu, L. D. Zhao, X. F. Tang, G. J. Tan, *Acta Mater.* **2021**, *220*, 117337.
[58] F. Li, M. Ruan, B. Jabar, C. B. Liang, Y. X. Chen, D. W. Ao, Z. H. Zheng, P. Fan, W. S. Liu, *Nano Energy* **2021**, *88*, 106273.
[59] K. Jin, J. Tiwari, T. Feng, Y. Lou, B. Xu, *Nano Energy* **2022**, *100*, 107478.
[60] A. V. Sotnikov, M. M. Syrokvashin, V. V. Bakovets, I. Yu Filatova, E. V. Korotaev, A. Sh Agazhanov, D. A. Samoshkin, *J. Am. Ceram. Soc.* **2022**, *105*, 2813–2822.

Manuscript received: August 31, 2022
Accepted manuscript online: September 19, 2022
Version of record online: October 7, 2022

© 2022 Wiley-VCH GmbH

15213773, 2022, 45, Downloaded from https://onlinelibrary.wiley.com/doi/10.1002/anie.202212885 by University Of Utah, Wiley Online Library on [14/11/2022]. See the Terms and Conditions (https://onlinelibrary.wiley.com/terms-and-conditions) on Wiley Online Library for rules of use; OA articles are governed by the applicable Creative Commons License

Angewandte Chemie
Eine Zeitschrift der Gesellschaft Deutscher Chemiker

Supporting Information

Realizing $zT > 2$ in Environment-Friendly Monoclinic Cu_2S—Tetragonal $Cu_{1.96}S$ Nano-Phase Junctions for Thermoelectrics

X. Li, Y. Lou, K. Jin, L. Fu, P. Xu, Z. Shi, T. Feng, B. Xu**

Experimental Procedures

Synthesis of the Cu_2S with ligand (DDT) (Synthesis of nanocrystal precursors): Cu $(CH_3COO)_2$ (6 g) was added to the mixed solution of 1-dodecanethiol (225 mL) and 1-dodecanol (75 mL) in a three-neck round-bottom flask. The mixture was heated to 230 ℃ and kept at this temperature for 60 min under N_2 protection and stirring. Finally, the solution was cooled down to ~ 70 ℃ naturally, isolated by centrifugation at 11000 rpm for 5 minutes, and washed with a mixture of 180 ml cyclohexane and 90 ml absolute ethanol. Finally, the samples were dried in a vacuum oven at 60 °C for 24 hours.

Spark plasma sintering (SPS) process： The powders were compacted into tablets (10 mm diameter; ~3 mm thickness). Then, the die was loaded into the Sinterland LabBox-110, and the temperature was increased to 200 ℃ with a heating rate of 100 ℃ min^{-1} and then increased to 450 ℃ in 15 minutes. Once the sample reached the designated temperature, the pressure was rapidly increased up to 50 MPa. The pellet was held under these conditions for 15 minutes and then cooled down naturally.

Synthesis of the $M_{0.9}T_{0.1}$: The dried precursor powders were heated to 723 K for 12 hours under a vacuum in a tube furnace and cooled down naturally. The final powders are sintered by the SPS process.

Synthesis of the $M_{0.78}T_{0.22}$: The synthesis procedure is the same as that of $M_{0.9}T_{0.1,}$ except that the dried powders were heated to 723 K for 3 hours under a vacuum in a tube furnace and then subjected to SPS.

Synthesis of the $M_{0.36}T_{0.64}$: The dried precursor powders were sintered by the SPS process without treatment by the tube furnace.

Synthesis of the $M_{0.34}T_{0.66}$: The dried precursor powders were exposed to air for five days and then sintered by the SPS process.

Synthesis of the $M_{0.31}T_{0.69}$: The washed precursor powders were re-dispersed in a three-neck round-bottom flask with 200 mL of cyclohexane and 200 ml of oleylamine for post-processing. The reaction temperature was set at 50 ℃, and the mixture was maintained for 60 min in an oil bath under N_2 protection and stirring. Subsequently, the solution was isolated by centrifugation at 11000 rpm for 5 minutes and washed with the mixture of 180 ml cyclohexane and 90 ml absolute ethanol. The samples were dried in a vacuum oven at 60 °C for 24 h. The dried powders are exposed to air for five days and then sintered by the SPS process.

Material Characterization. We performed electrical and thermal property measurements on the copper sulfide compounds parallel to the pressing direction. The cylindrical tablets were sectioned into bars of 9.50 mm × 3.00 mm× 3.00 mm for simultaneous measurements of the Seebeck coefficient (S) and electrical conductivity (σ) over 300-923 K using a Cryoall CTA-3 instrument. In addition, the samples were also sintered into tablets with a diameter of 10.00 mm and then coated with a thin layer of graphite for the thermal diffusivity (D) measurement over the same temperature range using a TA DXF-900 instrument. The thermal conductivity (κ_{tot}) was calculated using $\kappa_{tot} = D \times Cp \times \rho$, where the heat capacity (Cp) was measured on a NETZSCH STA449F3 differential scanning calorimetry (DSC) thermal analyzer from 300 to 923 K, and the sample density (ρ) was calculated from the mass and dimensions of the tablets. The zT values were obtained via $zT = S^2\sigma T/\kappa_{tot}$. Hall effects were performed on an HMS-7000 hall instrument under a reversible magnetic field of ±1 T using a Hall bar geometry. The chemical compositions of the $Cu_{2-x}S$ polished sintered tablets were characterized on a JXA-8530F Plus Hyper Probe electron probe microanalysis (EPMA) at 15 kV. Selected area electron diffraction (SAED) patterns and transmission electron microscopy (TEM) images were collected using a Thermo Fisher Scientific Talos F200S G2 microscope (acceleration voltage 200 kV) to characterize the structural features of the $Cu_{2-x}S$. Preparation of the TEM samples: the copper sulfide powders were dispersed in ethanol, and then several drops of the prepared suspension were dropped onto a holey C-coated Ni TEM grid. The thermogravimetric analysis (TGA) of powder samples was performed on a NETZSCH STA449F3 thermogravimetric analyzer from 323 K to 923 K with a heating rate of 10 K/min. The composition and chemical states of the samples were analyzed by X-ray Photoelectron Spectroscopy (XPS) on a Thermo Field Company's Thermo Scientific K-alpha instrument that uses Al-Kα micro-focusing monochromatic X-ray source (1486.6 eV). C 1s peak (284.8 eV) was used to calibrate peak positions. The Cu L-edge XANES spectra were measured at the BL12B-a beamline of the National Synchrotron Radiation Laboratory (NSRL) in China using total electron yield (TEY) mode. X-ray diffraction (XRD) patterns of sintered tablets were determined on a Bruker D8 Advance X-ray powder diffractometer with Cu Kα radiation (λ = 1.5418 Å) to record their crystal structures and component phases. Rietveld refinement was performed against the XRD patterns using the GSAS and EXPGUI software packages with the formerly reported Cu_2S and $Cu_{1.96}S$ structures as bases. The lattice parameters and weight fraction of each phase can be obtained.

Density functional theory calculation. The density functional theory was performed using Vienna ab initial simulation pack code (VASP) [1] via the projected plane waves method (PAW). [2] The tetragonal crystal structure (chemical formula: Cu_8S_4, space group: $P4_32_12$) and monoclinic (chemical formula: $Cu_{96}S_{48}$, space group: $P2_1/c$) phase Cu_2S were obtained from the Materials Project. [3] Considering the low concentration of Cu vacancy as experimental measured ($Cu_{1.97}S$), a 2 × 2 × 3 supercell for tetragonal phase Cu_2S was established to simulate the change of electronic structure with the increase of Cu vacancies. At the same time, the conventional cell of monoclinic phase Cu_2S is large enough (containing 144 atoms) to simulate the experimental concentration of Cu vacancy. The exchange-correlation energy was calculated using generalized gradient approximation (GGA) functional reported by Perdew, Burke, and Ernzerhof (PBE). [4] The Hubbard Coulomb energy term (U = 7 eV) was introduced to improve the localization characteristic of the 3d electrons of copper. [5] After cell optimization, the Hellmann-Feynman force of all the ions is less than 0.01 eV/Å. The kinetic energy cutoff is set as 400 eV, and the convergence of the energy of adjacent iteration is 10^{-7} eV in calculations of the density of states (DOS) and band structure. The Monk Horst-Pack [6] method was used to sample the reciprocal space. 8 × 8 × 2 and 4 × 6 × 4 k-meshes are

used in self-consistent field iteration sampling for tetragonal and monoclinic Cu_2S supercells, respectively. The paths of high symmetry points for band structure calculating in reciprocal space are Γ-X-M-Γ-Z-R-A-Z (tetragonal) and Γ-Z-D-B-Γ-A-E-Z-C_2-Y_2-Γ (monoclinic). For easy observation, the Fermi level is set to 0 eV. DOS and band structure data were extracted via VASPKIT code [7].

The formation energy of systems with Cu-vacancies is calculated by the following equation [8]: E_f [$Cu_{96-x}S_{48}$] = E_{total} [$Cu_{96-x}S_{48}$]-E_{total} [$Cu_{96}S_{48}$, bulk]-$n_{Cu}\cdot\mu_{Cu}$ +2 (E_f + E_{VBM}), where E_{total} is the total energy of the calculated system at 0 K, n is the number of defect atoms, μ is the chemical potential of corresponding particles, and E_f is the Fermi level. The chemical potential of Cu is -1.498 eV from DFT calculation with the same Hubbard parameter U.

All surfaces are modeled as being symmetric up and down, but this results in the chemical formula deviating from Cu_2S. We fixed the intermediate bulk part and relaxed the upper and lower surfaces of the Slab model, with the thickness of the surface exceeding 5 Å. The thickness of vacuum layers was set to 15 Å to avoid interference between the upper and lower surfaces. The surface energy was calculated from the formula below, $\gamma = (E_{slab} - N \times E_{bulk} - n_i \times \mu_i) / (2\alpha)$, where the γ is the surface energy of a certain (h k l) crystal plane, α is the area of that crystal plane, E_{slab} is the energy of the relaxed surface, E_{bulk} is the total energy of bulk sample, N is a coefficient to make the atom numbers of E_{bulk} less than or equal to E_{slab}, n_i is the number of excess Cu or S atoms after subtraction, and μ_i is its relative chemical potential. The calculated chemical possibilities of Cu and S are -1.498 eV and -4.127 eV, respectively.

The phonon dispersion relations were calculated using the Phonopy package [9] with VASP through density functional perturbation theory (DFPT) [10]. The convergency of Hellmann-Feynman forces is 10^{-6} eV/Å and 10^{-4} eV/Å for each atom in the tetragonal and monoclinic conventional cell, respectively. To eliminate negative frequency, a 3 × 3 × 2 supercell of tetragonal Cu2S (containing 216 atoms) was established. The Γ-centered k-meshes used in calculations were 2 × 2 × 1 and 2 × 2 × 2 for tetragonal and monoclinic phases, respectively. The path of the Brillouin region of the phonon spectrum is the same as that of the electronic band structure. The 8 × 8 × 8 and 25 × 25 × 9 sampling q-meshes are used to calculate the density of states, group velocity, and other thermal properties for tetragonal and monoclinic phases, respectively.

Results and Discussion

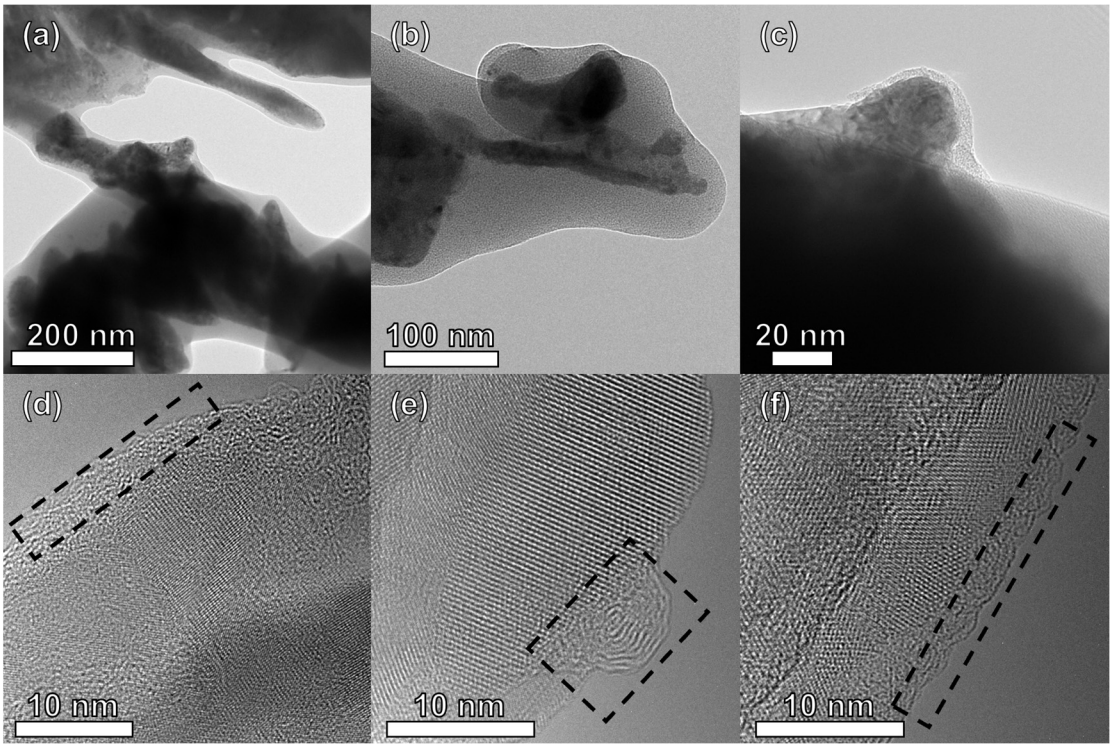

Figure S1. The DDT ligands were carbonized into carbon and coated on the grain of $M_{0.36}T_{0.64}$.

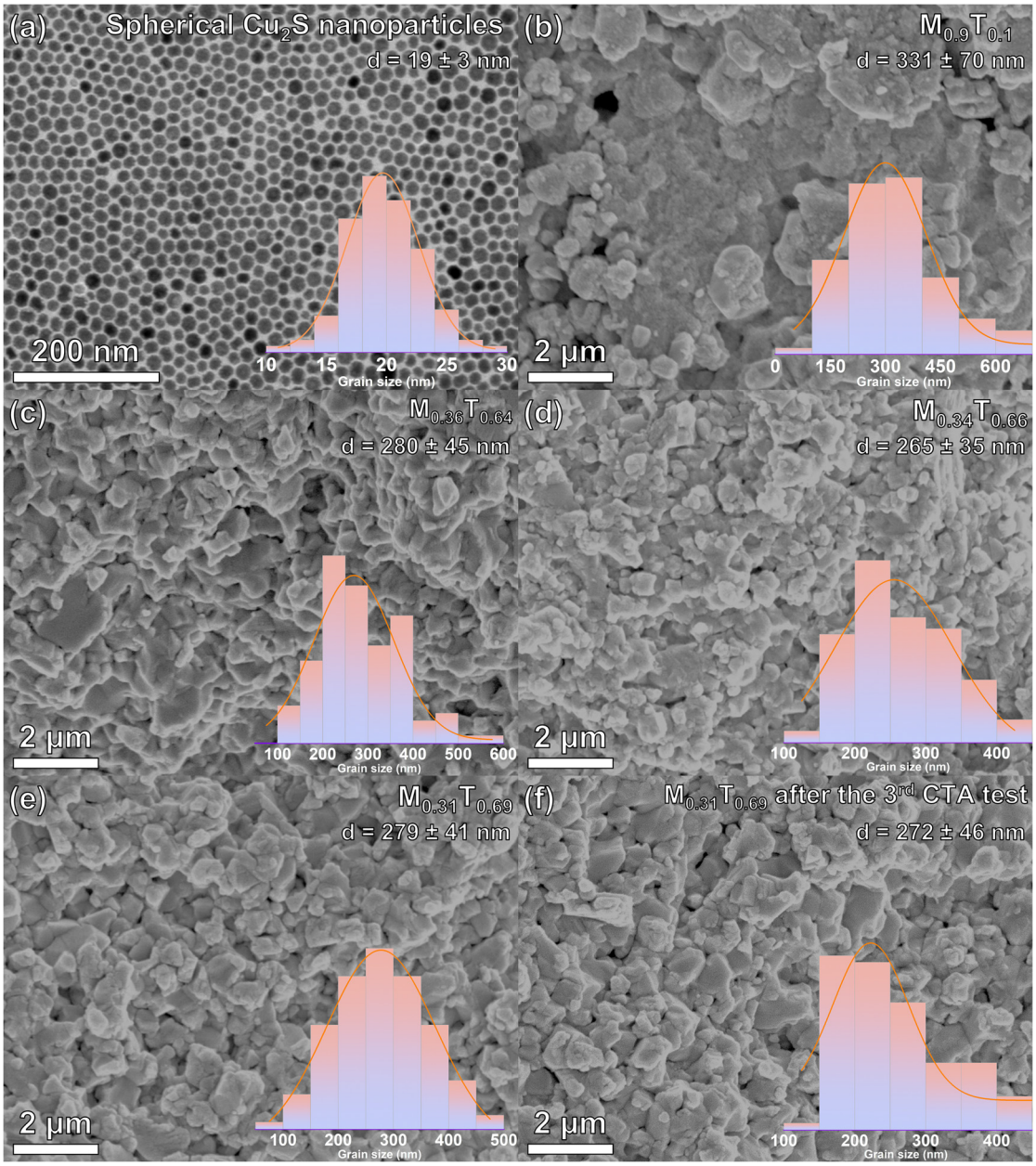

Figure S2. The SEM images inserted the grain size distributions histograms and the related average size (counting more than 100 particles) of (a) the as-synthesized spherical Cu_2S nanoparticles, (b) the $M_{0.9}T_{0.1}$, (c) the $M_{0.36}T_{0.64}$, (d) the $M_{0.34}T_{0.66}$, (e) the $M_{0.31}T_{0.69}$, and (f) the $M_{0.31}T_{0.69}$ after the third CTA test.

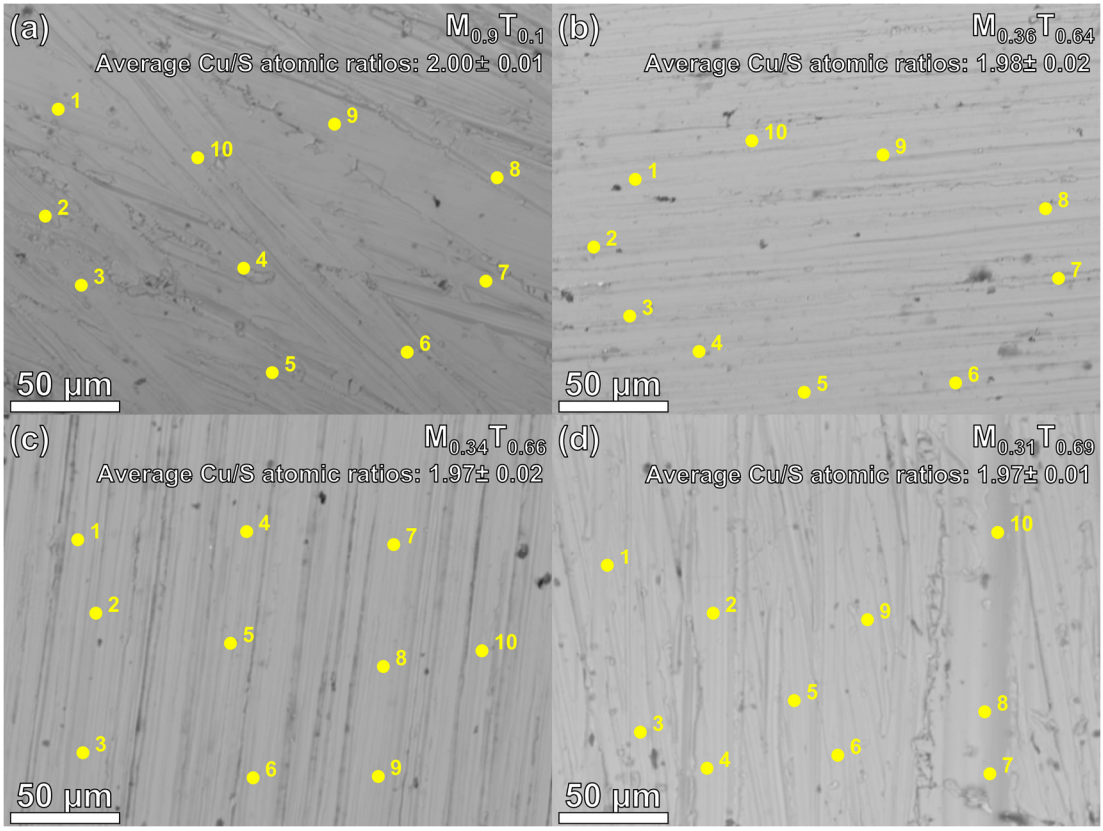

Figure S3. (a) the $M_{0.9}T_{0.1}$, (b) the $M_{0.36}T_{0.64}$, (c) the $M_{0.34}T_{0.66}$, and (d) the $M_{0.31}T_{0.69}$ bulk materials tested by WDS in EPMA.

Table S1. Element content based on WDS

Sample	Cu/S atomic ratios									
	Point 1	Point 2	Point 3	Point 4	Point 5	Point 6	Point 7	Point 8	Point 9	Point 10
$M_{0.9}T_{0.1}$	2.018	1.994	1.999	1.991	1.998	2.032	2.008	1.990	1.978	2.001
$M_{0.36}T_{0.64}$	1.974	2.065	1.971	1.973	1.972	1.983	1.974	1.985	1.974	1.982
$M_{0.34}T_{0.66}$	1.975	1.969	2.062	1.973	1.969	1.968	1.887	1.969	1.974	1.976
$M_{0.31}T_{0.69}$	1.953	1.968	1.970	1.972	1.985	1.950	1.962	1.952	1.967	1.966

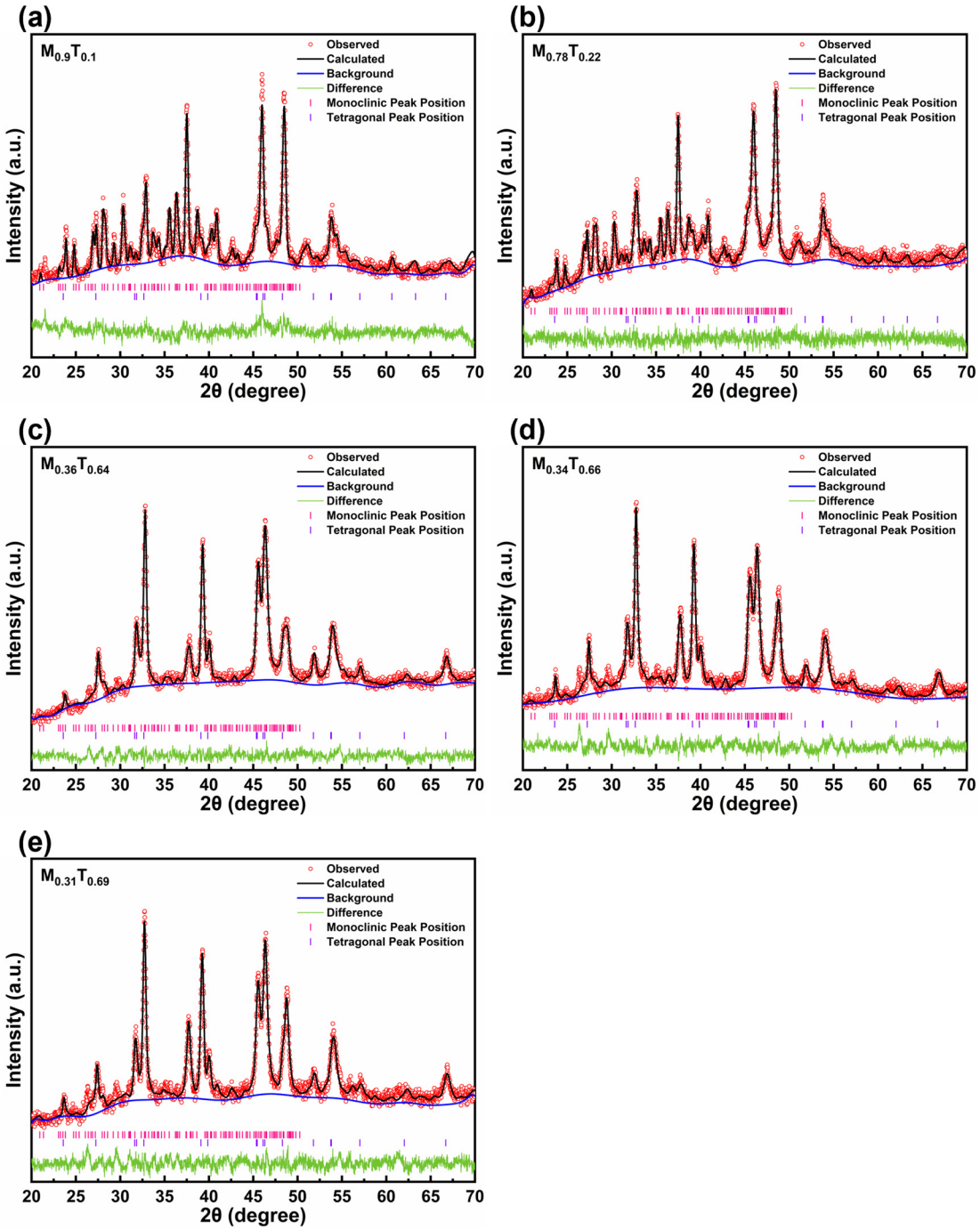

Figure S4. Rietveld refinement with XRD pattern of (a) the $M_{0.9}T_{0.1}$, (b) the $M_{0.78}T_{0.22}$, (c) the $M_{0.36}T_{0.64}$, (d) the $M_{0.34}T_{0.66}$, and (d) the $M_{0.31}T_{0.69}$.

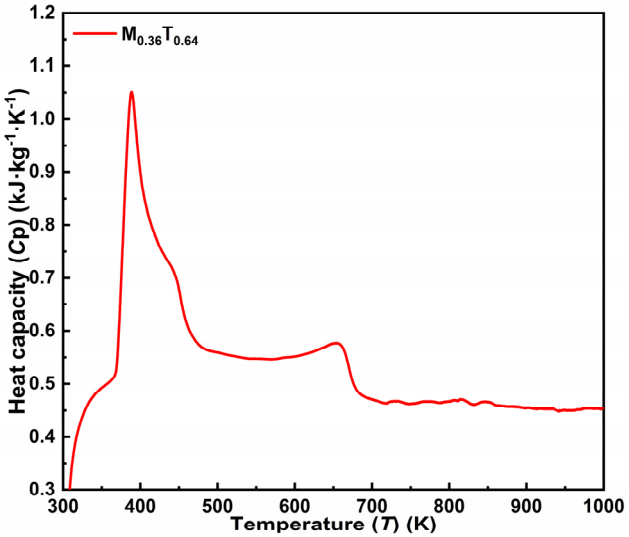

Figure S5. The differential scanning calorimetry (DSC) curve of the $M_{0.36}T_{0.64}$.

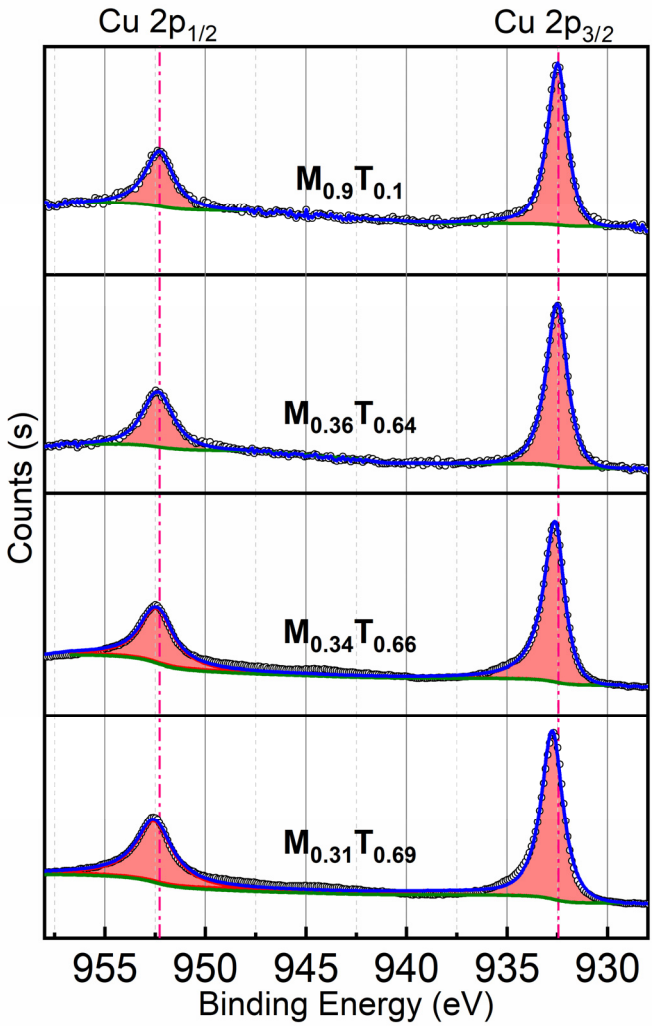

Figure S6. The XPS peak areas of Cu $2p_{1/2}$ and $2p_{3/2}$ of the $M_{0.9}T_{0.1}$, $M_{0.36}T_{0.64}$, $M_{0.34}T_{0.66}$, and $M_{0.31}T_{0.69}$.

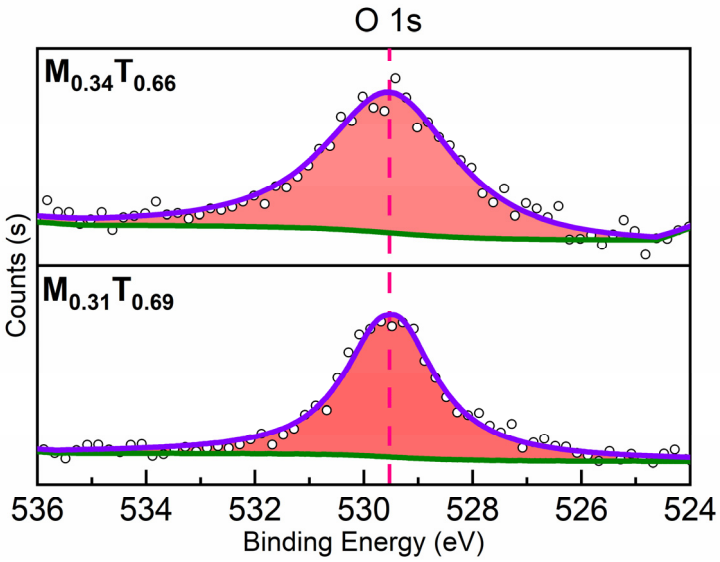

Figure S7. The XPS peak areas of O 1s of the $M_{0.34}T_{0.66}$ and $M_{0.31}T_{0.69}$.

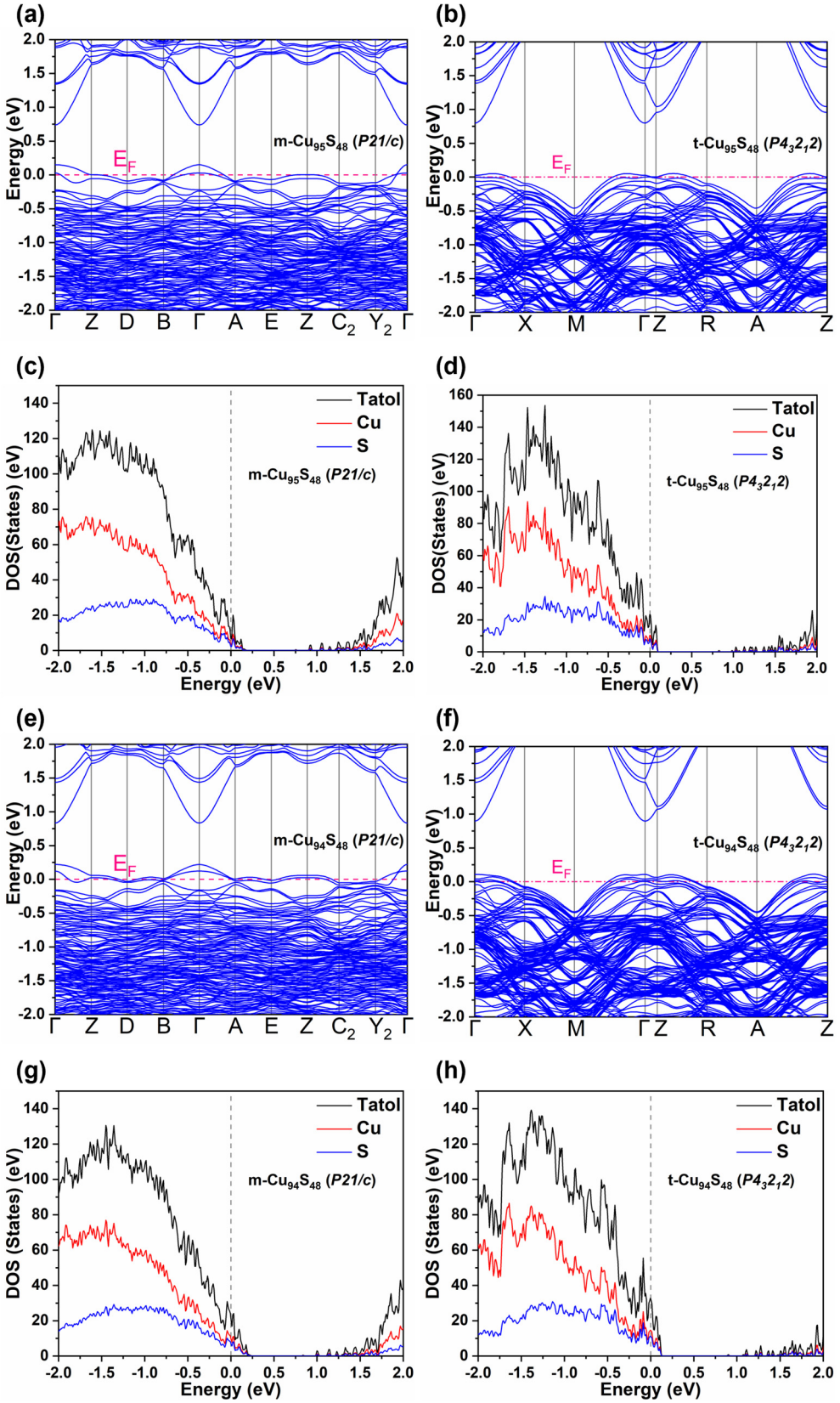

Figure S8. GGA+ U calculated the electronic band structure of (a) m-$Cu_{96}S_{48}$ (V_{Cu}-free m-Cu_2S) with $P2_1/c$ structure, (b) m-$Cu_{94}S_{48}$ (m-Cu_2S with $2V_{Cu}$) with $P2_1/c$ structure, (c) t-$Cu_{96}S_{48}$ (V_{Cu}-free t-$Cu_{1.96}S$) with $P4_32_12$ structure, and (d) t-$Cu_{94}S_{48}$ (t-$Cu_{1.96}S$ with $2V_{Cu}$) with $P4_32_12$ structure. (e) and (f) Electronic band structure and DOS of m-$Cu_{95}S_{48}$ (m-Cu_2S with $1V_{Cu}$) with $P2_1/c$ structure. (g) and (h) Electronic band structure and DOS of t-$Cu_{95}S_{48}$ (t-$Cu_{1.96}S$ with $1V_{Cu}$) with $P4_32_12$ structure.

Table S2. Comparison of calculated total (E_{total}) and formation energies (ΔE_f) of monoclinic Cu_2S and tetragonal $Cu_{1.96}S$ with different content of V_{Cu}.

Situation	E_{total} (eV)	ΔE_f (eV)	ΔE_f (eV/atom)
m-$Cu_{96}S_{48}$ (V_{Cu}-free m-Cu_2S)	-385.53	——	——
m-$Cu_{95}S_{48}$ (m-Cu_2S with 1V_{Cu})	-383.80	-3.227	-0.023
m-$Cu_{94}S_{48}$ (m-Cu_2S with 2V_{Cu})	-381.80	-6.721	-0.047
t-$Cu_{96}S_{48}$ (V_{Cu}-free t-$Cu_{1.96}S$)	-385.01	——	——
t-$Cu_{95}S_{48}$ (t-$Cu_{1.96}S$ with 1V_{Cu})	-382.87	-3.641	-0.025
t-$Cu_{94}S_{48}$ (t-$Cu_{1.96}S$ with 2V_{Cu})	-380.85	-7.162	-0.050

Table S3. The calculated surface energies (γ) of different crystallographic facets and particle-averaged surface energy ($\bar{\gamma}$) of monoclinic Cu_2S and tetragonal $Cu_{1.96}S$.

Situation	Surface (h k l)	γ (J/m^2)	$\bar{\gamma}$ (J/m^2)
m-$Cu_{96}S_{48}$ (V_{Cu}-free m-Cu_2S)	(1 0 0)	0.413	0.389
	(0 1 0)	0.330	
	(0 0 1)	0.441	
	(1 -1 0)	0.431	
	(-1 0 -1)	0.329	
t-$Cu_{96}S_{48}$ (V_{Cu}-free t-$Cu_{1.96}S$)	(1 0 0)	0.265	0.329
	(0 0 1)	0.349	
	(1 0 1)	0.257	
	(1 0 4)	0.283	
	(1 1 1)	0.557	

Table S4. The density of state (DOS) effective mass (m_d*) of m-Cu_2S and t-$Cu_{1.96}S$.

Situation	Direction	m_l or m_t	m_d*
m-Cu_2S	Γ → Z	1.75 m_e	0.76 m_e
	Γ → H	1.99 m_e	
	Γ → Y_2	0.13 m_e	
t-$Cu_{1.96}S$	Γ → Z	0.20 m_e	1.34 m_e
	Γ → X	3.45 m_e	

Note: In the k_x-k_y-k_z coordinate system of the Brillouin zone, k_x, k_y, and k_z are perpendicular to each other. In m-Cu_2S, k_z is taken as the Γ → Z direction of the monoclinic Brillouin zone, k_x as the Γ → H direction, and k_y as the Γ → Y_2 direction; in t-$Cu_{1.96}S$, k_z is taken as the Γ → Z direction of the tetragonal Brillouin zone, k_x as the Γ → X direction, and k_y as the Γ → X direction; the effective mass in the k_z direction is m_l, and the effective mass in the k_x and k_y directions is m_t; $m_d^* = (m_l \cdot m_t^2)^{1/3}$.

Table S5. Thermal conductivity simulation from the phonon dispersion relation of m-Cu_2S and t-$Cu_{1.96}S$[a].

Situation	$\kappa_{lat,x}$($W \cdot m^{-1} \cdot K^{-1}$)	$\kappa_{lat,y}$($W \cdot m^{-1} \cdot K^{-1}$)	$\kappa_{lat,z}$($W \cdot m^{-1} \cdot K^{-1}$)
m-Cu_2S	0.150	0.131	0.142
t-$Cu_{1.96}S$	0.467	0.467	0.385

[a] Assuming that the grain size is small, the mean free path (MFP) of phonons should be the same as the grain size.

Table S6. Thermal conductivity simulation from the phonon dispersion relation of m-Cu_2S and t-$Cu_{1.96}S$[b].

Situation	$\kappa_{lat,x}$($W \cdot m^{-1} \cdot K^{-1}$)	$\kappa_{lat,y}$($W \cdot m^{-1} \cdot K^{-1}$)	$\kappa_{lat,z}$($W \cdot m^{-1} \cdot K^{-1}$)
m-Cu_2S	0.38	0.45	0.36
t-$Cu_{1.96}S$	4.05	4.05	1.99

[b] Assuming a large and pure crystal, the phonon lifetime is Constant·ω^{-2}.

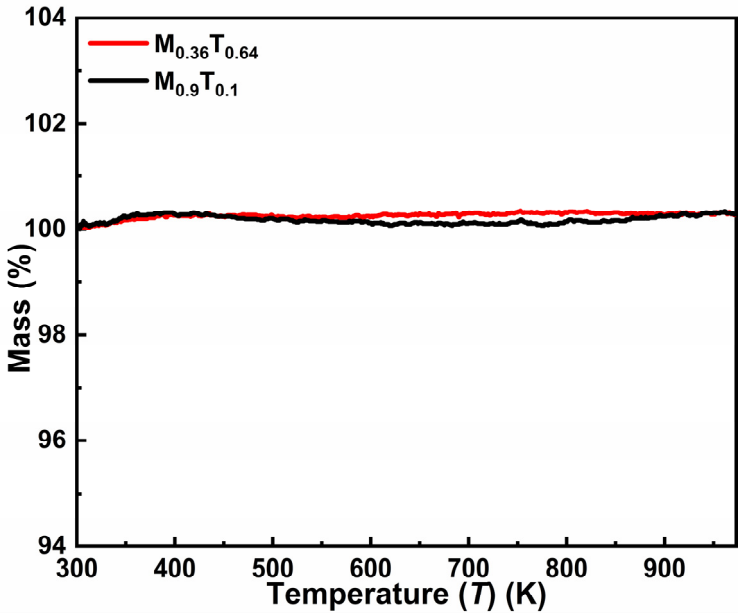

Figure S9. Thermogravimetric analysis (TGA) of $M_{0.9}T_{0.1}$ and the $M_{0.36}T_{0.64}$. The weight losses of both samples are less than 1%.

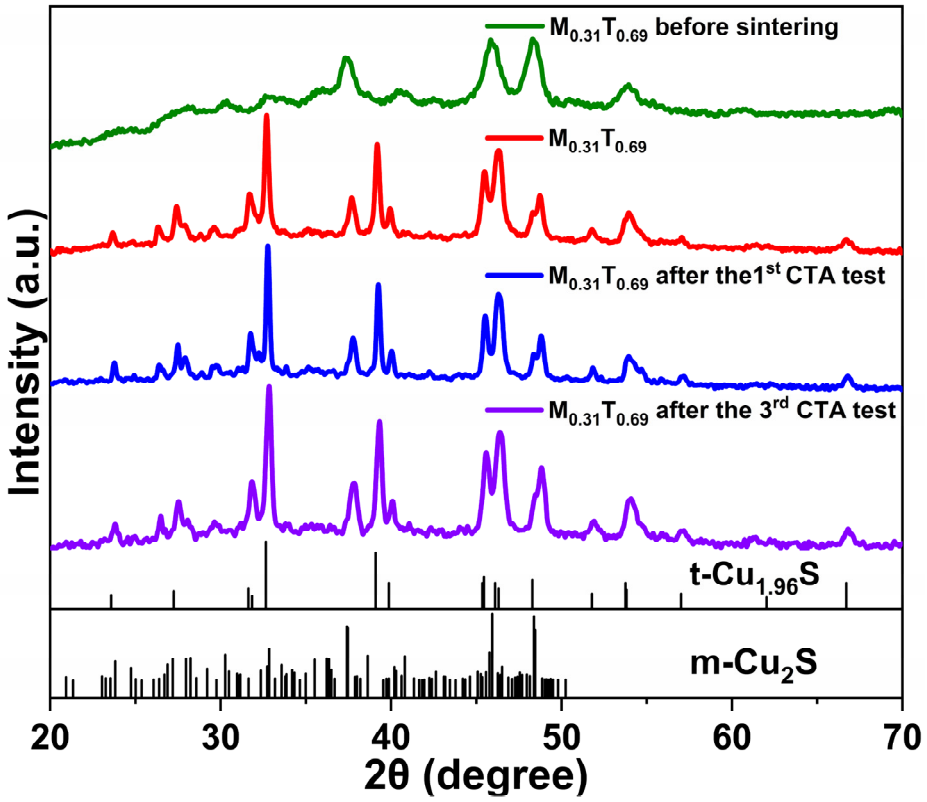

Figure S10. XRD patterns after different stages of electrical performance cycling tests.

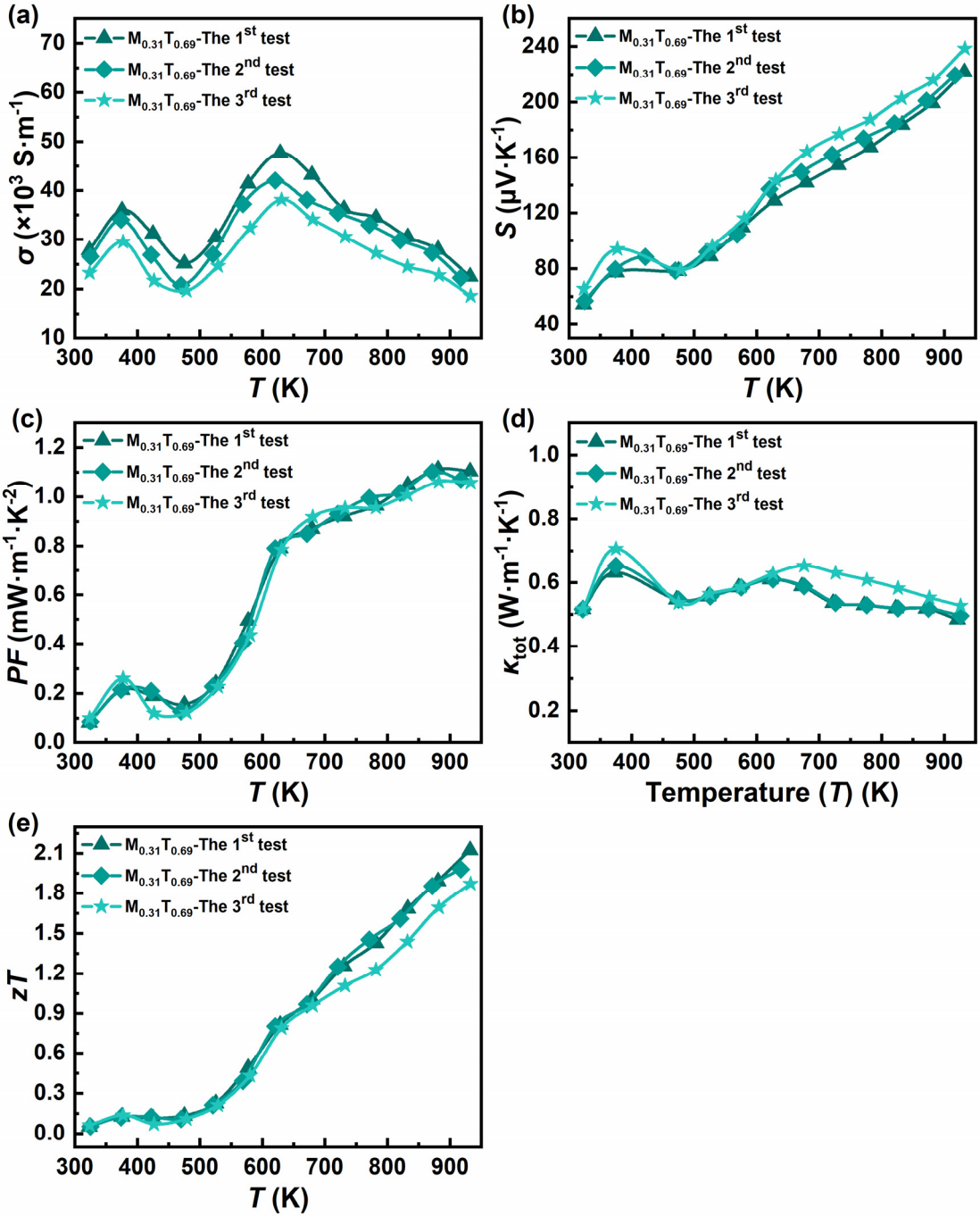

Figure S11. Temperature-dependent thermoelectric properties in the cyclic test of $M_{0.31}T_{0.69}$: (a) Electric conductivity, (b) Seebeck coefficient, (c) Power factor, (d) Thermal conductivity, and (e) zT values.

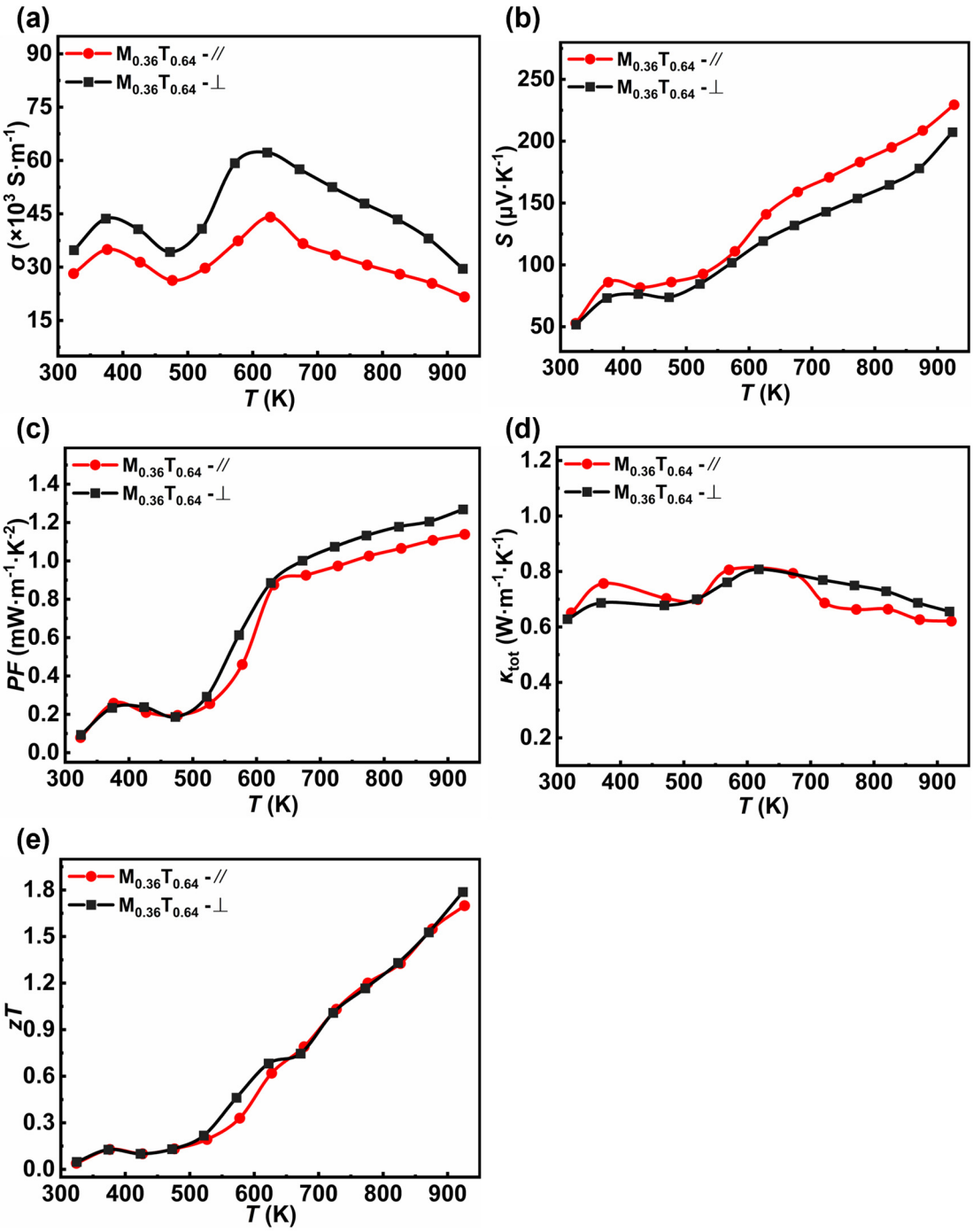

Figure S12. Temperature-dependent thermoelectric properties in the anisotropic test of $M_{0.36}T_{0.64}$: (a) Electric conductivity, (b) Seebeck coefficient, (c) Power factor, (d) Thermal conductivity, and (e) zT values.

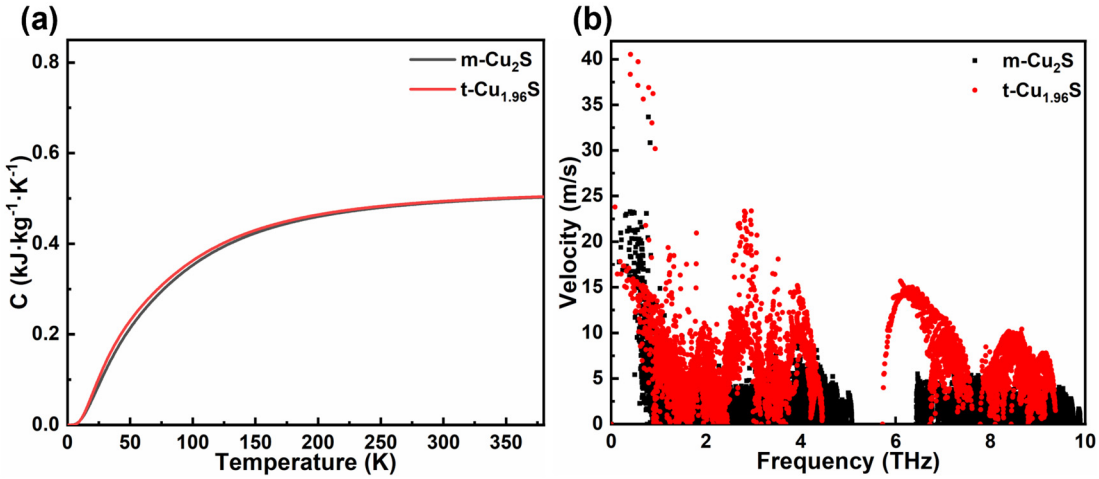

Figure S13. (a) the phonon heat capacity (*c*) comparison, and (b) the phonon group velocity comparison(*v*) between m-Cu_2S and t-$Cu_{1.96}S$.

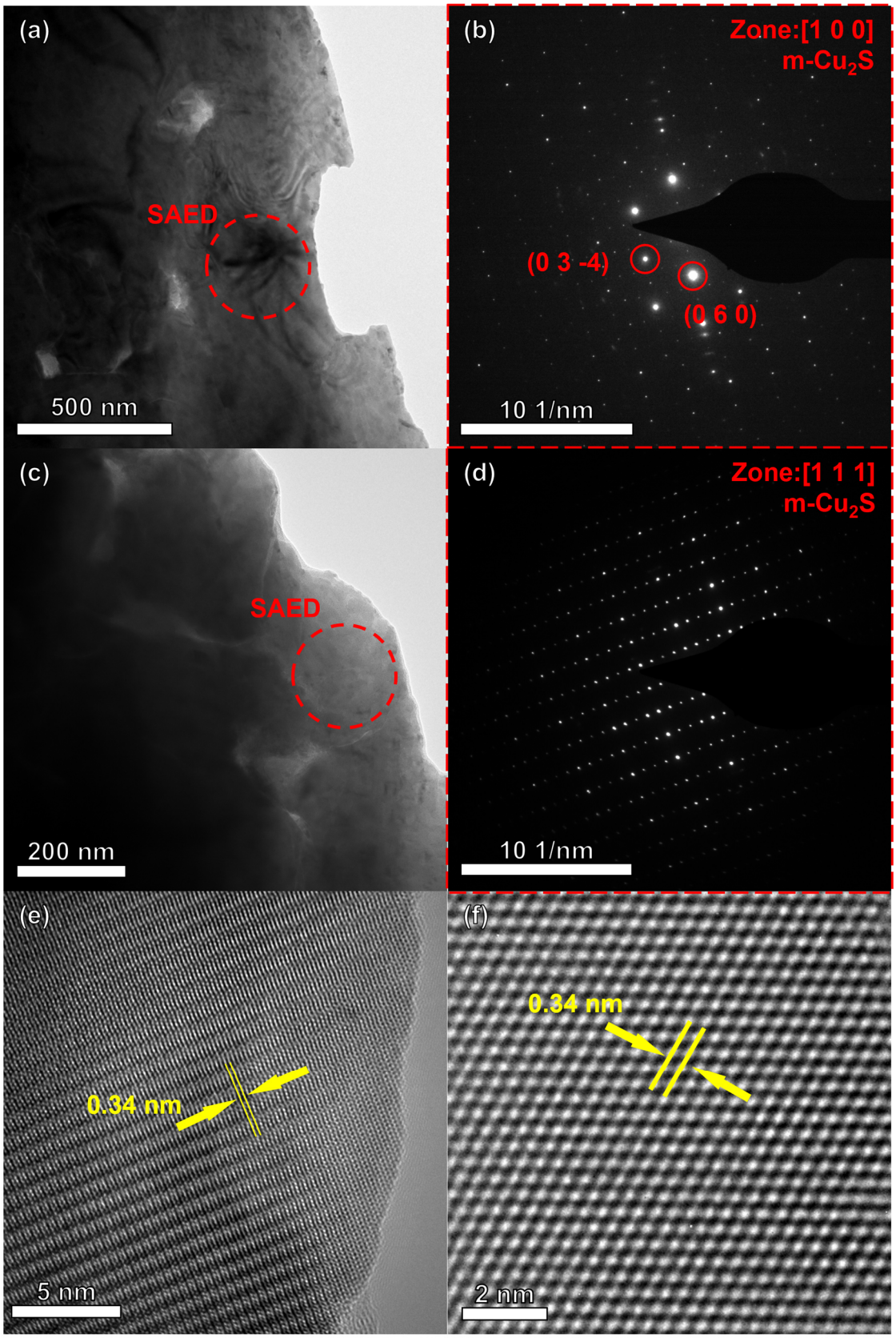

Figure S14. (a, c) The TEM images of the $M_{0.9}T_{0.1}$ sample, (b, d) the corresponding selected area electron diffraction (SAED) patterns of red dotted boxes in (a, c), respectively, and (e, f) the TEM images of $M_{0.9}T_{0.1}$ sample.

Nanocrystal Cu_2S with oxidation treatment for different days and nanocrystal Cu_2S treated with oleylamine and then oxidized for different days are explored. Experimental results are shown in Figures S15 and S16, and the samples are labeled "air-day *n*" and "OAm-air-day *n*," respectively. The material $M_{0.36}T_{0.64}$ discussed in our manuscript, which was neither exposed to air nor reacted with OAm, corresponds to "air-day 0". The material $M_{0.34}T_{0.66}$, which has not reacted with OAm but was exposed to air for 5 days, corresponds to "air-day 5". The material $M_{0.31}T_{0.69}$, which was not only reacted with OAm but also exposed to air for 5 days, corresponds to "OAm-air-day 5".

As shown in Figures S15 and S16, the thermoelectric properties of samples exhibit the same trend with the increase of days of oxidation. In the first five days, Seebeck increases with increasing oxidation days while the conductivity decreases, which leads to a decrease in final *PF*. At the same time, the total thermal conductivity decreases at a greater rate, which causes the *zT* to increase every day for the first five days of oxidation until a maximum value is reached. After the sixth day of oxidation, the electrical conductivity is still deteriorating while the thermal conductivity is no longer decreasing, which causes the *zT* to fall back on the sixth day of oxidation. The electrical conductivity decreases because the Cu_2O produced through air oxidation can provide scattering for the charge carriers, reducing the carrier mobility μ_H and thus the electrical conductivity. For thermal conductivity, the decrease in conductivity leads to a decrease in electronic thermal conductivity. The Cu_2O generated by constant oxidation continuously enhances the scattering of phonons, thus reducing the lattice thermal conductivity. Although the Cu_2O negatively affects electronic carrier mobility slightly, a higher proportion of the corresponding reduction in thermal conductivity compensates and leads to the optimized Figure-of-merit *zT* of air-day 0 ($M_{0.36}T_{0.64}$) and $M_{0.31}T_{0.69}$ (OAm-air-day 5).

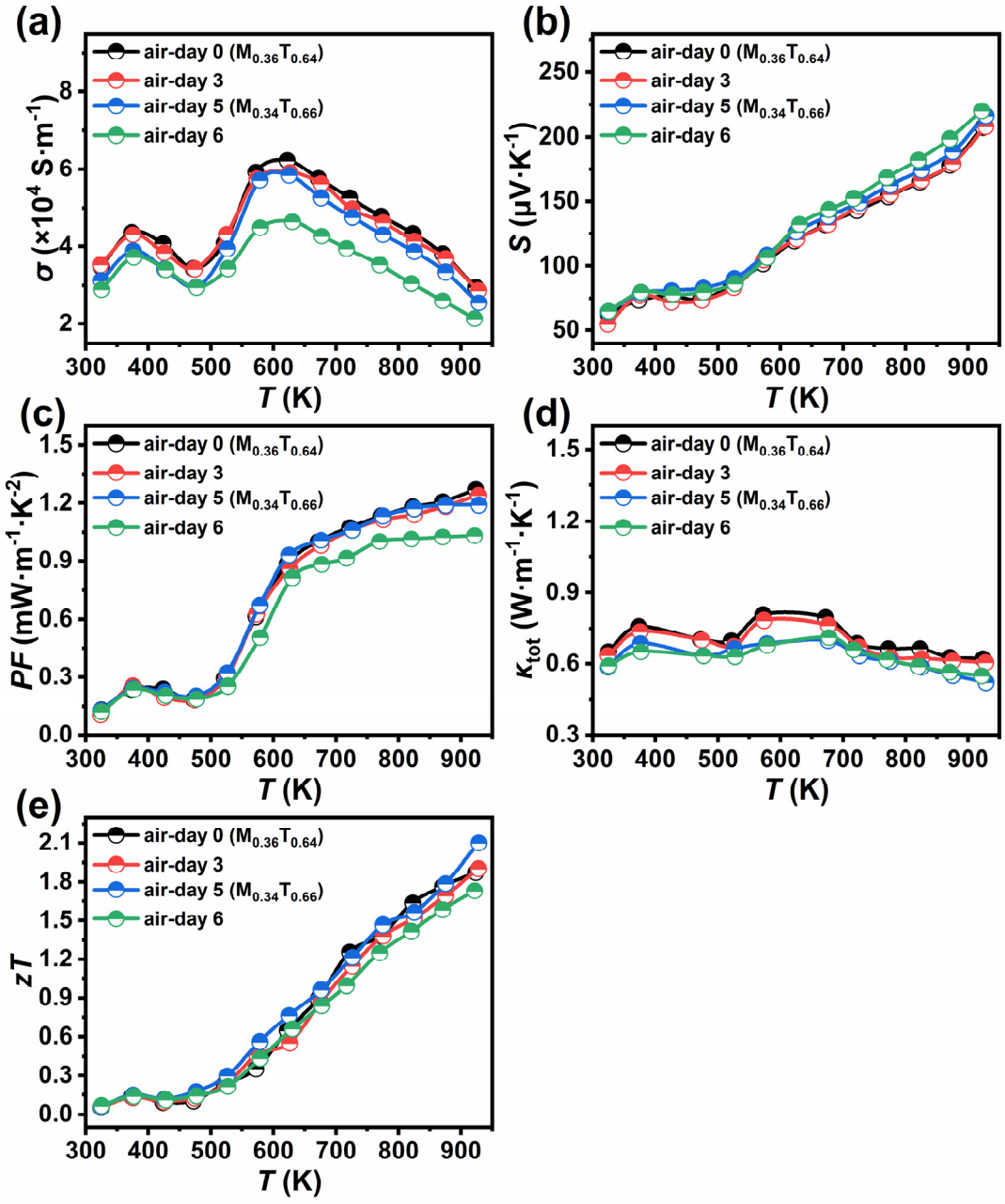

Figure S15. Temperature-dependent thermoelectric properties of "air-day 0", "air-day 3", "air-day 5", and "air-day 6": (a) electric conductivity, (b) Seebeck coefficient, (c) power factor, (d) thermal conductivity, and (e) *zT* values.

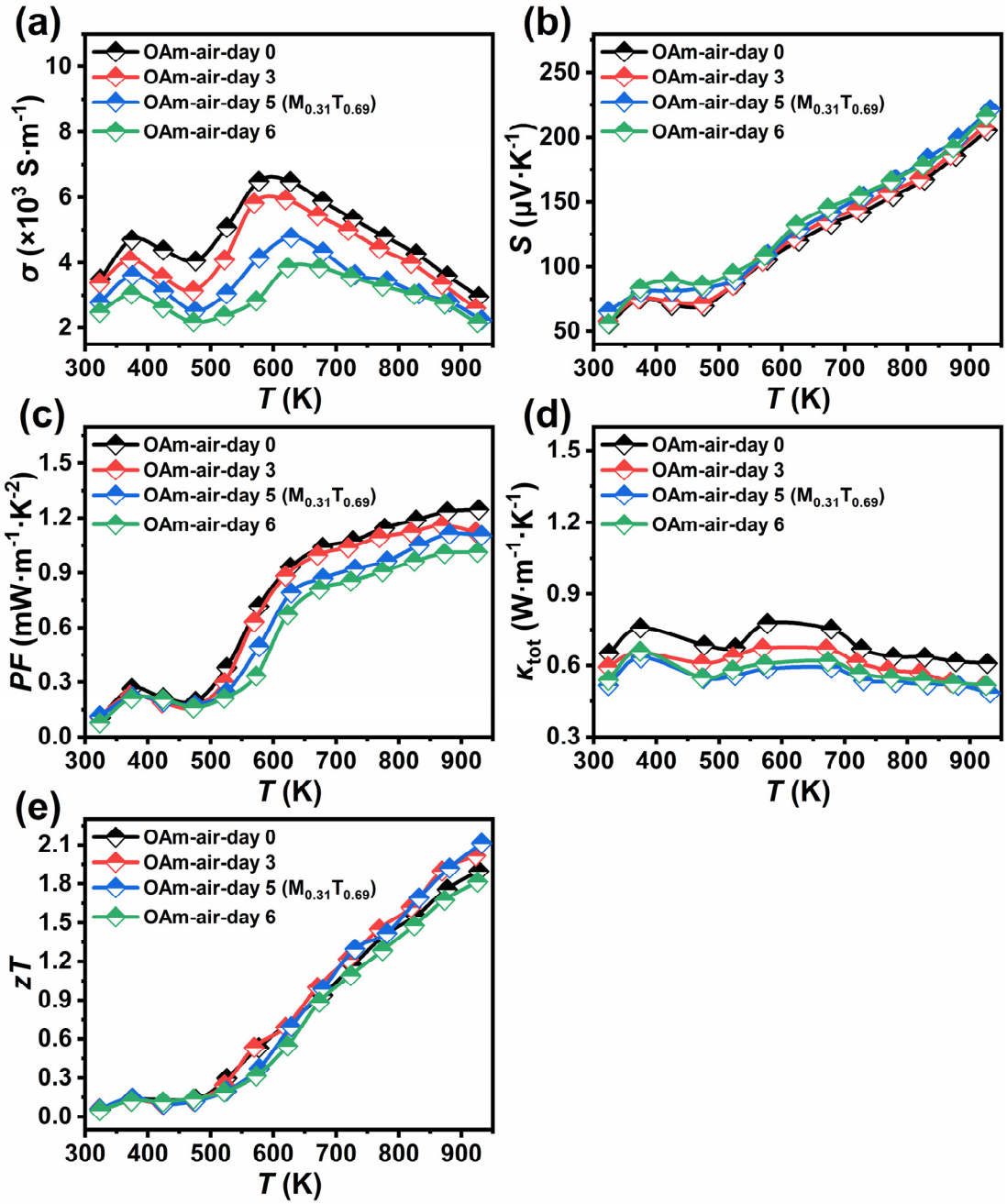

Figure S16. Temperature-dependent thermoelectric properties of "OAm-air-day 0", "OAm-air-day 3", "OAm-air-day 5", and "OAm-air-day 6": (a) electric conductivity, (b) Seebeck coefficient, (c) power factor, (d) thermal conductivity, and (e) *zT* values.

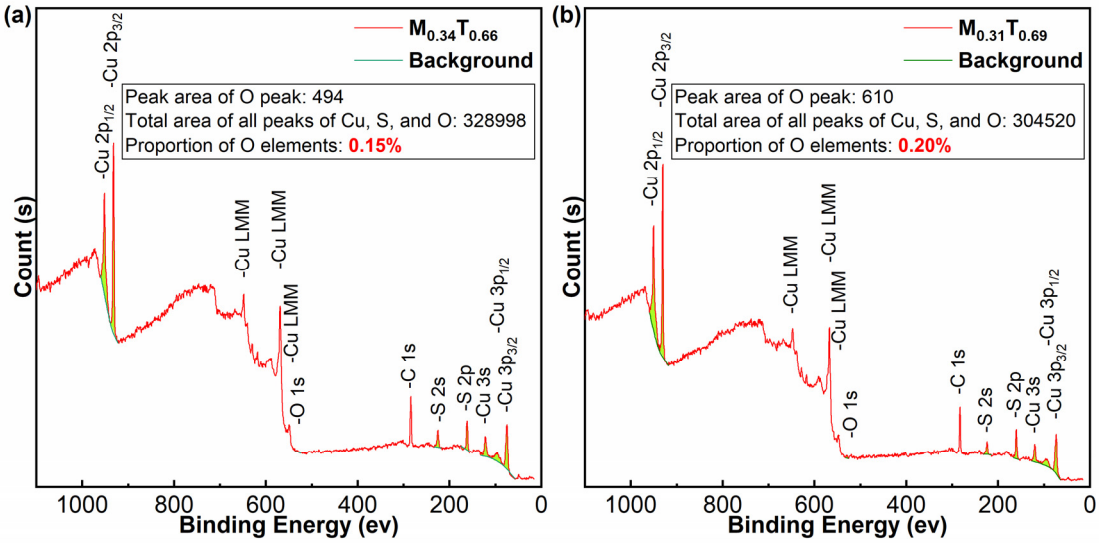

Figure S17. (a) XPS full-spectrum sweep of (a) $M_{0.34}T_{0.66}$ and (b) $M_{0.31}T_{0.69}$. The sum of the green areas in (a) and (b) represents the sum of the peak areas of all elements (Cu, S, and O) in $M_{0.34}T_{0.66}$ and $M_{0.31}T_{0.69}$, respectively.

The content of carbon for $M_{0.36}T_{0.64}$ (1.45 wt%) and $M_{0.9}T_{0.1}$ (0.128 wt%) (Table S7) was tested by a carbon and sulfur automatic analyzer (HIR-944, Wuxi High-Speed Analytical Instrument Co., Ltd.).

Table S7. The content of carbon for $M_{0.36}T_{0.64}$ and $M_{0.9}T_{0.1}$

Sample	The content of carbon (wt%)
$M_{0.36}T_{0.64}$	1.450
$M_{0.9}T_{0.1}$	0.128

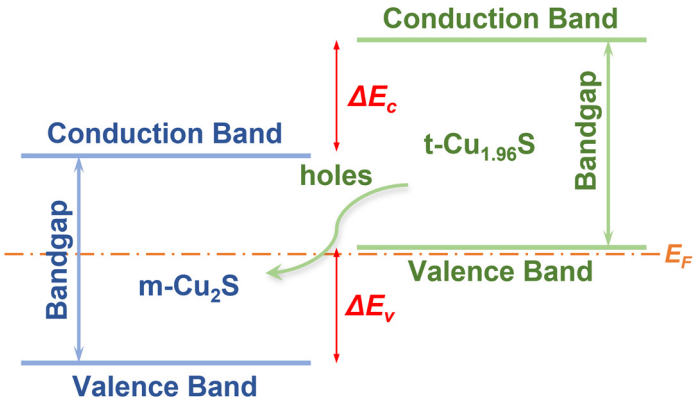

Figure S18 The t-$Cu_{1.96}S$ on m-Cu_2S band alignment.

References

[1] G. Kresse, J. Furthmuller, *Phys. Rev. B: Condens. Matter Mater. Phys.* **1996**, *54*, 11169-11186.
[2] P. E. Blochl, *Phys. Rev. B: Condens. Matter Mater. Phys.* **1994**, *50*, 17953-17979.
[3] A. Jain, S. P. Ong, G. Hautier, W. Chen, W. D. Richards, S. Dacek, S. Cholia, D. Gunter, D. Skinner, G. Ceder, K. A. Persson, *APL Mater.* **2013**, *1*, 011002.
[4] J. P. Perdew, K. Burke, M. Ernzerhof, *Phys. Rev. Lett.* **1996**, *77*, 3865-3868.
[5] J. M. Fernández-Díaz, S. L. Palacios, A. Menéndez-Blanco, *J. Appl. Phys.* **2020**, *128*, 084904.
[6] H. J. Monkhorst, J. D. Pack, *Phys Rev B* **1976**, *13*, 5188-5192.
[7] V. Wang, N. Xu, J.-C. Liu, G. Tang, W.-T. Geng, *Comput. Phys. Commun.* **2021**, *267*, 108033.
[8] C. Freysoldt, B. Grabowski, T. Hickel, J. Neugebauer, G. Kresse, A. Janotti, C. G. Van De Walle, *Rev. Mod. Phys.* **2014**, *86*, 253-305.
[9] A. Togo, I. Tanaka, *Scr. Mater.* **2015**, *108*, 1-5.
[10] S. Baroni, S. De Gironcoli, A. Dal Corso, P. Giannozzi, *Rev. Mod. Phys.* **2001**, *73*, 515-562.

Author Contributions

+ These two authors contributed equally